Elongasome core proteins and class A PBP1a display zonal, processive movement at the midcell of *Streptococcus pneumoniae*

Amilcar J. Perez[a1], Melissa M. Lamanna[a1], Kevin E. Bruce[a1], Marc A. Touraev[a], Julia E. Page[b], Sidney L. Shaw[a], Ho-Ching Tiffany Tsui[a], and Malcolm E. Winkler[a2]

[a]Department of Biology, Indiana University Bloomington, Bloomington, IN 47405; [b]Department of Microbiology, Blavatnik Institute, Harvard Medical School, Boston, MA 02115

[1]A.J.P., M.M.L. and K.E.B. contributed equally to this work.

Running title: Dynamics of pneumococcal peripheral PG synthesis

Key words: processive movement of PG synthesis proteins; PBP2b:RodA:MreC elongasome dynamics; Class A PBP circumferential movement; MpgA muramidase confined subdiffusion; diffusion of non-active PG synthesis proteins

[2]Corresponding author:

Malcolm E. Winkler
Department of Biology
Indiana University Bloomington
1001 East Third Street
Bloomington, Indiana 47405 USA
Phone: 812-856-1318
Email: winklerm@indiana.edu

ABSTRACT

Ovoid-shaped bacteria, such as *Streptococcus pneumoniae* (pneumococcus), have two spatially separated peptidoglycan (PG) synthase nanomachines that locate zonally to the midcell of dividing cells. The septal PG synthase bPBP2x:FtsW closes the septum of dividing pneumococcal cells, whereas the elongasome located on the outer edge of the septal annulus synthesizes peripheral PG outward. We showed previously by sm-TIRFm that the septal PG synthase moves circumferentially at midcell, driven by PG synthesis and not by FtsZ treadmilling. The pneumococcal elongasome consists of the PG synthase bPBP2b:RodA, regulators MreC, MreD, and RodZ, but not MreB, and genetically associated proteins Class A aPBP1a and muramidase MpgA. Given its zonal location separate from FtsZ, it was of considerable interest to determine the dynamics of proteins in the pneumococcal elongasome. We found that bPBP2b, RodA, and MreC move circumferentially with the same velocities and durations at midcell, driven by PG synthesis. However, outside of the midcell zone, the majority of these elongasome proteins move diffusively over the entire surface of cells. Depletion of MreC resulted in loss of circumferential movement of bPBP2b, and bPBP2b and RodA require each other for localization and circumferential movement. Notably, a fraction of aPBP1a molecules also moved circumferentially at midcell with velocities similar to those of components of the core elongasome, but for shorter durations. Other aPBP1a molecules were static at midcell or diffusing over cell bodies. Last, MpgA displayed non-processive, subdiffusive motion that was largely confined to the midcell region and less frequently detected over the cell body.

SIGNIFICANCE

These results demonstrate that unlike in rod-shaped bacteria, the core elongasome of *S. pneumoniae* exhibits zonal, circumferential motion. This motion is independent of FtsZ treadmilling or the presence of MreB filaments and is separate from the circumferential motion of the septal PG synthase that closes the septal annulus. Also unlike in rod-shaped bacteria, a Class A PBP moves processively at midcell, distinctly from components of the core PG elongasome or septal PG synthase. Thus, processive, circumferential motion in pneumococcal cells follows spatially separate linear tracks that may reflect a common ordered structure in the existing peptidoglycan itself. In contrast, the MpgA muramidase displays a different kind of subdiffusive motion that is largely confined to midcell by an unknown mechanism.

INTRODUCTION

The peptidoglycan (PG) cell wall protects bacteria from osmotic stress, determines cell shape, size, and chaining critical for adaptation and host interactions, and serves as a scaffolding in Gram-positive bacteria for the attachment of wall-teichoic acids, capsules, and extracellular enzymes and virulence factors (1-5). PG synthesis has provided targets for a large number of clinically relevant antibiotics and remains one of the most fertile sources for the discovery of new antibiotic targets in drug-resistant pathogens (6-11). Although a general picture of PG synthesis has emerged (12-16), many fundamental questions remain unanswered about the composition, coordination, chronology, and regulation of the nanomachines that carry out PG synthesis in bacteria. Moreover, major differences have recently emerged in how different bacteria carry out PG synthesis and

use homologous proteins in different ways (see (17-23)). *Streptococcus pneumoniae* (pneumococcus; *Spn*) has emerged as a model for PG synthesis in ovoid-shaped bacteria that is tractable to genetic, biochemical, and cell biological approaches (reviewed in (4, 24, 25)). *S. pneumoniae* is a human nasopharyngeal commensal bacterium that becomes a serious opportunistic pathogen, killing over one million people annually worldwide (26-28). Moreover, *S. pneumoniae* is an antibiotic-resistant "superbug," for which new antibiotic targets are urgently needed (10, 29-31).

Unlike in rod-shaped bacteria, all PG synthesis is zonal and confined to a band at the middle of dividing *S. pneumoniae* cells (Fig. S1) (24, 32, 33). At the start of cell division, the septal and elongation (peripheral) PG synthesis nanomachines locate to an FtsZ ring at the equators of predivisional daughter cells (Fig. S1*A*) (34, 35). Unlike *Bacillus subtilis* and *Staphylococcus aureus* (36-39), septal ring closure and cell separation occur simultaneously during the *S. pneumoniae* cell cycle, as do septal and elongation PG synthesis, with elongation PG synthesis likely starting slightly before septal PG synthesis in the initial FtsZ ring (24, 32, 33, 35, 40). As septation progresses, the septal and elongation PG synthesis nanomachines physically separate to the inside and outside edges, respectively, of the midcell annular disk (Fig. S1*B* and S1*C*) (24, 33, 41). Septal PG synthesis in the inner ring, which contains FtsZ and the Class B bPBP2x:FtsW (SEDS) complex, separates the dividing cells (24, 32-35). Elongation PG synthesis, which is carried out by the pneumococcal core elongasome in the outer ring (24, 32, 33), emanates outward and has been postulated to push MapZ-nascent FtsZ/FtsA/EzrA rings toward the equators of new daughter cells (Fig. S1*A*) (34, 42, 43). Notably, *S. pneumoniae* lacks Min and Noc systems (44, 45) and forms FtsZ rings over the nucleoid (22, 46, 47).

97 Consequently, dividing pneumococcal cells characteristically contain three FtsZ rings
98 throughout most of division, one at the closing septum and two in the developing
99 equatorial rings (Fig. S1*A*) (34, 46, 48). Interestingly, proteins that mediate bundling FtsZ
100 filaments, such as SepF, ZapA, and ZapJ (ZipA is absent), arrive to the equatorial rings
101 very late in cell division (34, 41, 49).

102 Septal ring closure is zonal and confined to a midcell ring in many bacteria (50-52).
103 Dynamics studies showed that the pneumococcal bPBP2x:FtsW PG septal synthase
104 moves circumferentially at midcell driven by PG synthesis itself, and not by FtsZ
105 treadmilling (34), as was initially concluded for *B. subtilis* (53). Recent papers
106 demonstrate that zonal septal closure is indeed driven by circumferential septal PG
107 synthesis in *Escherichia coli* (54), *S. aureus* (55), and *B. subtilis* (56), rather than by FtsZ
108 treadmilling.

109 However, elongation PG synthesis in rod-shaped cells is not zonal but is distributed
110 along the curved cylindrical body of growing cells (57-59). This synthesis is carried out by
111 the Rod-complex elongasome consisting of MreB and the PG elongasome complex.
112 Actin-like MreB polymerizes into multiple short, curved filaments perpendicular to the cell
113 long axis along the cell membrane, which is the region of maximal negative Gaussian
114 curvature (16, 60-62). MreB interacts with the cytoplasmic helix-turn-helix domain of the
115 bitopic RodZ protein that also interacts with the elongasome PG synthase complex facing
116 outside the cell membrane (62-65). The core elongasome consists of the polytopic shape,
117 elongation, division and sporulation (SEDS) family protein RodA (glycosyltransferase;
118 GT), an essential bitopic Class B bPBP (transpeptidase; TP), and bitopic and polytopic
119 positive regulators MreC and MreD, respectively (16, 66-70). Similar to septal PG

synthesis, movement of the assembled Rod elongasome is driven by side-wall PG synthesis itself, rather than by ATPase-dependent treadmilling of MreB (57-59). Thus, MreB filaments serve as curvature-sensing “rudders” for processive synthesis of separate parallel strands of side-wall PG (61). In addition, Class A PBPs, which are bitopic proteins with extracellular GT and TP activities, move largely in non-ordered paths and often stop, possibly filling in or reinforcing gaps left by the Rod system (16, 71-74).

In contrast to rod-shaped bacteria, pneumococcal elongasome PG synthesis is zonal and confined to the initial FtsZ ring and later to the outer edge of the septal annular disk (24, 32, 33). The core pneumococcal elongasome contains RodA, Class B bPBP2b, RodZ, MreC, and MreD, but does not contain an MreB homolog (19, 25, 35, 46, 75-79). RodZ(*Spn*) serves as an organizer of elongasome assembly and is required for MreC midcell localization followed by localization of RodA and bPBP2b (19, 80). Immunofluorescence microscopy (IFM) indicated that Class A aPBP1a and the MpgA muramidase co-localize with bPBP2b and MreC, but not with bPBP2x, throughout the cell cycle, including after the outer elongasome PG synthesis ring forms at midcell (Fig. S1) (35, 46, 80). Thus, aPBP1a and MpgA localize with peripheral PG synthesis, although it has not been determined whether they are persistent members of the core elongasome.

Paradoxically, the absence of aPBP1a suppresses the requirement for MreCD and RodZ (80, 81), whereas inactivation of *pbp1b*, which encodes Class A aPBP1b, suppresses the requirement for RodZ, but not for MreCD (19). In both cases, the bPBP2b:RodA PG synthase is still required for viability, suggesting that the absence of aPBP1a or aPBP1b may activate bypass pathways that obviate the requirement for certain regulators of the core elongasome (19, 80). However, amino acid changes that

143 reduce the catalytic activity of the MpgA muramidase (80, 82) abolish the requirement for
144 the entire pneumococcal PG elongasome, including the bPBP2b:RodA PG synthase (24,
145 80). The CozE protein was also implicated in pneumococcal elongation PG synthesis
146 (83). However, CozE did not behave equivalently to MreCD in transformation assays of
147 function (84), and the exact function of pneumococcal CozE remains unknown. A
148 pneumococcal TseB homolog renamed as CopD was recently reported to bind to bPBP2b
149 and aPBP1a. Absence of CopD produces wider cells, consistent with a defect in
150 elongation PG synthesis (85); however, the mechanism underlying this morphology
151 change is not known. Last, FtsX is located with the outer ring elongasome proteins later
152 in pneumococcal division (32). FtsX is a subunit of the FtsEX:PcsB PG hydrolase that is
153 thought to play an essential role in PG remodeling between septal and peripheral PG (86-
154 89). Notably, the FtsX(*Bsu*) homolog is also associated with side-wall PG synthesis (90,
155 91).

156 In this paper, we show that the pneumococcal bPBP2b, RodA, and MreC core
157 elongasome proteins move circumferentially with the same velocity and processivity at
158 midcell at different division stages. Unless indicated otherwise, midcell refers to the
159 central rings at the septa of dividing cells and to the equators of predivisional daughter
160 cells about to start division. The processive movement of the core elongasome
161 components is driven by PG synthesis, and is not affected by FtsZ treadmilling, consistent
162 with the absence of FtsZ in the outer ring of elongasome PG synthesis later in division.
163 Strikingly, at WT protein expression levels in exponentially growing cells, a large majority
164 of bPBP2b, RodA, and MreC molecules diffuse in the membrane over the body of
165 pneumococcal cells without synthesizing PG. Unexpectedly, Class A aPBP1a also moves

166 circumferentially at midcell with a similar velocity, but in shorter tracks, than the core
167 elongasome components. Processive movement of aPBP1a at midcell depended on PG
168 synthesis, and again, a majority of aPBP1a molecules were found diffusing over the cell
169 body without synthesizing PG. Finally, the MpgA muramidase showed a distinctive
170 pattern of non-processive, subdiffusive movement, largely confined to midcell regions.
171 These results demonstrate that the pneumococcal PG elongasome moves zonally, which
172 is different from elongasome movement in rod-shaped bacteria, that a Class A PBP
173 moves circumferentially as well as diffusively, and that a PG hydrolase shows unusual
174 fast non-processive movement confined largely to the midcell region. The implications of
175 these modes of movement to the functions of the pneumococcal PG elongasome, Class
176 A PBPs, and PG muramidases and to patterns of PG-glycan strand placement are
177 discussed.
178

179 **RESULTS**

180 **Construction of functional fluorescent-protein fusions.** Fusions to pneumococcal
181 elongasome proteins bPBP2b, RodA, MreC, aPBP1a, and MpgA, were constructed at
182 native chromosomal loci to contain an N-terminal expression-enhancing "i-tag", fused to
183 an intracellular HaloTag (HT) domain, followed by a 15 amino-acid linker, fused to the
184 protein of interest (Tables S1 and S2), as described previously (32, 34, 92-95). Growth of
185 strains expressing iHT-fused proteins in C+Y, pH 6.9 medium was indistinguishable from
186 that of WT (Fig. S2*A*). Localization of iHT-fused proteins labeled with saturating amounts
187 of HT-TMR ligand matched previously published localization patterns of epitope-tagged
188 or GFP-fused proteins imaged by IFM or two-dimensional epifluorescence microscopy

189 (2D-FM), respectively (Fig. S2*B*) (19, 32, 34, 35, 42, 46, 80, 81, 85, 96). Western blots of
190 these fusions with intracellular iHT domains probed with antibody to native MreC,
191 bPBP2b, aPBP1a, or MpgA showed expression of full-length fusions with minimal
192 cleavage of the iHT domain (Figs. S3*A*, S4*B*, S5*B* and S6). In contrast, western blots of
193 an extracellular C-terminal HT fusion to MreC (MreC-HT) probed with anti-MreC antibody
194 showed extensive cleavage of the HT domain not detectable in blots probed with anti-HT
195 antibody (Fig. S3*A*, middle and right). Cleavage of extracellular HT domains was also
196 reported in *E. coli* (97), and our results emphasize the need to validate protein fusion
197 stability in blots with antibody to native proteins.

198 We reported previously that some tagged proteins, such as iHT-bPBP2b and sfGFP-
199 bPBP2b, were expressed from their chromosomal locus in significantly lower amounts
200 than WT bPBP2b in cells grown in BHI broth, with only minor effects on cell growth and
201 morphology under this growth condition (32). We observed similar results for cells grown
202 in C+Y, pH 6.9 medium, which is required for live-cell fluorescence microscopy (34). The
203 cellular amounts of iHT-bPBP2b and iHT-aPBP1a were 15 ± 5% and 10 ± 10% (mean
204 ±SD) of the WT bPBP2b and aPBP1a amounts, respectively (Fig. S4*B* and S5*B*; Table
205 S3). Underproduced iHT-bPBP2b caused minor increases in cell width and size (Fig. S4
206 *C* and *D*). However, the reduced amount of iHT-aPBP1a partly phenocopied a Δ*pbp1a*
207 mutant (Fig. S5 *C* and *D*). The cellular amounts of iHT-MreC and iHT-MpgA expressed
208 from their chromosomal loci were 82 ±18% and 171 ± 11% of the WT MreC and MpgA
209 amounts, respectively (Figs. S3*A* and S6; Table S3). Cells expressing iHT-MreC showed
210 minimal cell morphology differences from WT (Figs. S2*B* and S3*B*).

211 To increase cellular amounts of iHT-bPBP2b, iHT-aPBP1a, and iHT-RodA (antibody
212 to native RodA was not available), we constructed merodiploid strains in which each iHT-
213 tagged protein was also expressed from an ectopic site under the control of a zinc-
214 inducible promoter (98). Addition of Zn inducer ([$ZnCl_2$] indicated + 1/10 [$MnSO_4$] to
215 reduce zinc toxicity (41, 80, 99)) to cultures of these merodiploid strains did not affect
216 growth (Figs. S4*A* and S5*A*). Zn addition complemented the low cellular amounts of iHT-
217 bPBP2b and iHT-aPBP1a back up to 82 ± 6% and 101 ± 41% of the WT bPBP2b and
218 aPBP1a amounts, respectively (Figs. S4*B* and S5*B*; Table S3). Complementation also
219 alleviated minor cell shape defects detected in strains with reduced protein amounts
220 (Figs. S4*C* and *D*, S5*C* and *D*, and S7). iHT-fused proteins localized strongly to midcell
221 of Zn-induced merodiploid strains, but were also more dispersed over bodies of cells
222 compared to haploid or uninduced merodiploid strains (Figs. S4*C* and S5*C*). Finally,
223 merodiploid strains expressing iHT-bPBP2b or iHT-RodA showed minimal amounts of
224 cleavage products when 0.2 mM or 0.25 mM Zn inducer was added to the growth medium
225 (Figs. S4*B* and S7*B*). Effects of protein amounts on dynamics are described below.

226 **bPBP2b, RodA, and MreC display similar processive circumferential motion at**
227 **midcell.** Strains expressing functional iHT-fused proteins were labeled with limiting
228 concentrations of HT-JF549 ligand (Table S4), and single-molecule total internal
229 reflection fluorescence microscopy (sm-TIRFm) was performed for 180 s, as described
230 previously (34) (*Materials and Methods*). Three criteria were used to determine different
231 motion types. Processive circumferential motion was defined as a molecule moving in
232 one direction for more than six consecutive frames (imaging rate = 1 frame per second
233 (FPS)), with a linear velocity of ≥ 5 nm/s determined by kymograph analysis (Fig. 1*A*;

234 *Materials and Methods*). Static molecules were defined as being visible for more than six
235 consecutive frames with a velocity < 5 nm/s. Diffusively moving molecules were defined
236 as moving, but not in a consistent direction, for 6 or more non-consecutive frames within
237 a period of 90 s.

238 Single molecules of iHT-bPBP2b, iHT-RodA, and iHT-MreC displayed similar
239 processive circumferential motion exclusively at midcell (Fig. 1*A* and S8 and Movies S1
240 to S3), that resembled the circumferential motion of iHT-bPBP2x and FtsW-HT reported
241 previously (34). The frequency of circumferential, static, and diffusive molecules was
242 compiled for each strain (Fig. 1*B*). Examination of the circumferential tracks showed that
243 73% (54/74) of iHT-bPBP2b and 74% (57/77) of iHT-MreC molecules moved
244 unidirectionally at midcell. The remaining 27% of iHT-bPBP2b or 26% of iHT-MreC
245 molecules moved in one direction for at least six consecutive frames and then reversed
246 direction and moved in the opposite direction for at least six frames at approximately the
247 same velocity (angle in kymograph; Fig. 1*A*, right). Slow or non-moving static molecules
248 were mainly detected at midcell (Fig. S8), whereas diffusive molecules displayed rapid,
249 erratic movement throughout the cell (Fig. 1*B* and S8 and Movies S1 to S3). Fewer than
250 5% of molecules of these core elongasome proteins were observed to transition between
251 movement states (e.g., static to diffusive or circumferential).

252 **A limited number of bPBP2b, RodA, and MreC molecules engage in active PG**
253 **synthesis.** The distribution of single-molecule movement states of iHT-bPBP2b and iHT-
254 RodA was highly dependent on cellular protein levels. When expressed at 15% of the WT
255 level, ≈60% of iHT-bPBP2b moved circumferentially and only 32% moved diffusively (Fig.
256 1*B* and Movie S1). The remaining 7% of iHT-bPBP2b molecules were static, mainly at

257 midcell. iHT-RodA molecules expressed from the native locus showed a similar
258 distribution, suggesting that iHT-RodA was underproduced (Fig. 1*B* and Movie S2).
259 However, when iHT-PBP2b and iHT-RodA protein amounts were increased by ectopic
260 expression (to ≈82% the WT level for iHT-bPBP2b), only 16% or 9% of single iHT-bPBP2b
261 or iHT-RodA molecules, respectively, moved circumferentially, while ≈70% moved
262 diffusively, with the remaining 12% iHT-bPBP2b or 23% iHT-RodA static, mostly at
263 midcell (Fig. 1*B* and Movies S4 and S5). Uninduced merodiploid strains expressing iHT-
264 bPBP2b or iHT-RodA displayed movement distributions similar to those of haploid strains
265 (Fig. 1*B*). The amount iHT-MreC expressed from its native locus was nearly (82%) that
266 of WT (Fig. S3*A* and Table S3). Approximately 24% of iHT-MreC molecules moved
267 circumferentially, while 52% moved diffusively and 24% were static, similar to the
268 movement distributions of iHT-bPBP2b and iHT-RodA when they were ectopically
269 expressed (Fig. 1*B* and Movie S3).

270 High-resolution 3D structured-illumination microscopy (3D-SIM) on fixed cells
271 corroborated conclusions based on movement distributions. At protein amounts
272 corresponding to ≈15% of WT, iHT-bPBP2b localized primarily to regions of active PG
273 synthesis at midcell and equators of dividing cells, as indicated by HADA fluorescent D-
274 amino-acid labeling (Fig. 2*A*). When expressed near the WT level, iHT-bPBP2b remained
275 at the HADA-labeled midcell and equators but was mostly dispersed over the body of the
276 entire cell where HADA labeling was not detected (Fig. 2*B*). These results support the
277 conclusion that iHT-PBP2b molecules that move diffusively in the cell membrane outside
278 of midcell and equators are not actively synthesizing PG (Fig. 2*B*). Control experiments
279 using a GFP fusion construct to bPBP2b and labeling with a different fluorescent D-amino

acid (TADA) gave similar results (Fig. S9). 2D-FM images also showed an increase in dispersed iHT-bPBP2b localization when protein expression was increased to near the WT amount (Fig. S4*C*). We conclude that at any given time, a limited number of bPBP2b, RodA, and MreC molecules display processive circumferential motion at midcell where PG synthesis occurs. Conversely, bPBP2b, RodA, and MreC are expressed in excess in WT cells, and most molecules are diffusing over the cell surface and not synthesizing PG in cells under these and other growth conditions (Figs. 1*B*, 2*B* and S4*C*; Table S3) (32).

bPBP2b, RodA, and MreC form a stable elongasome complex that undergoes circumferential motion. If bPBP2b, RodA, and MreC form an elongasome complex, we would expect that each molecule would move with the same velocity. To test this idea, velocities of circumferentially moving molecules were determined by kymograph analysis (Fig. 3*A*) (34). The length of time these molecules were observed moving circumferentially, referred to here as the circumferential duration, was also measured (Fig. 3*B*), and the particle distance each circumferential molecule moved was calculated by multiplying the velocity by the duration (Fig. S10*A*). When expressed near WT levels (+Zn in merodiploid and haploid *mreC* constructs) the mean circumferential velocities, durations, and particle distances of iHT-bPBP2b, iHT-RodA, and iHT-MreC were statistically the same, at ≈11 nm/s, ≈23 s, and ≈230 nm, respectively (Fig. 3*A* and *B*; Fig. S10*A*). Additional strains containing different fusion constructs of bPBP2b and RodA moved at similar circumferential velocities (Fig. S11). These data support the idea that bPBP2b, RodA, and MreC form a stable, circumferentially moving elongasome complex at midcell.

302 **Circumferential movement of bPBP2b and RodA is independent of FtsZ**
303 **treadmilling and driven by PG synthesis.** Circumferential movement of the
304 pneumococcal septal PG synthase was shown to be independent of FtsZ treadmilling and
305 driven by PG synthesis {Perez, 2019 #136}. A similar conclusion was later reported for
306 the septal PG synthases of *S. aureus* (55) and *B. subtilis* (56) and for the population of
307 active septal PG synthases in *E. coli* (54, 100). In early divisional cells, the pneumococcal
308 PG elongasome is located in an FtsZ-ring that also contains the septal PG synthase (Fig.
309 S1*A*), whereas at later stages of division, the elongasome separates from the FtsZ-ring
310 and locates to the outer edge of the septal annular disk (Fig. S1 *B* and *C*) (24, 32, 33).
311 Notably, the same circumferential velocity of core elongasome protein iHT-MreC, which
312 was expressed near the WT level (Fig. S3*A*), was detected at equators of early divisional
313 cells, before ostensible constriction, and in later-divisional cells with clear constrictions,
314 when septal (inner) and elongasome (outer) rings are separated at midcell (32) (Figs.
315 S1*B* and S10*B*). Since the pneumococcal PG elongasome is initially in an FtsZ ring, we
316 tested whether iHT-bPBP2b velocity is decreased when FtsZ treadmilling is greatly
317 reduced by ectopic expression of GTPase mutant FtsZ(D214A), which reduces FtsZ
318 treadmilling velocity from ≈32 nm/s to ≈4 nm/s (34). To the contrary, overproduction of
319 FtsZ(D214A) caused a statistically minimal increase in iHT-bPBP2b velocity (Fig. 4*A* and
320 Movie S6), with a marginal decrease in growth rate (Fig. S12). Consistent with a lack of
321 dynamic coupling, the treadmilling velocity of FtsZ-sfGFP filaments was ≈2.4-fold greater
322 than the circumferential velocity of iHT-bPBP2b single molecules expressed in the same
323 cell (Fig. 4*B*; Movie S7). We conclude that circumferential movement of the
324 pneumococcal PG elongasome is independent of FtsZ treadmilling.

325 Two lines of evidence indicate that pneumococcal PG elongasome circumferential
326 movement is driven by PG synthesis. First, we determined iHT-bPBP2b or iHT-RodA
327 circumferential velocity in a Δ*murZ* (previously called Δ*murA1*) mutant, which lacks the
328 predominant MurZ homolog that catalyzes the first committed step of PG precursor
329 synthesis (34, 101). The circumferential velocity of iHT-bPBP2b or iHT-RodA was
330 substantially reduced by ≈1.6-fold in the Δ*murZ* mutant compared to WT (Fig. 4 *C* and *D*,
331 Movies S8 and S9). Previously, we showed that the velocity of FtsZ treadmilling is
332 unchanged in the Δ*murZ* mutant (34). Together, these results demonstrate that the rate
333 of midcell elongasome movement is dependent on PG synthesis precursor amounts.

334 Second, catalytic mutants of bPBP2b TP or RodA GT activity did not exhibit
335 processive, circumferential movement. No β-lactam antibiotic is known that preferentially
336 inhibits bPBP2b alone (102). Both bPBP2b and RodA are essential in *S. pneumoniae* (35,
337 75, 103). Consequently, we constructed merodiploid strains with *iht-pbp2b*(S391A) (TP
338 catalytic mutation) or *iht-rodA*(D283A) (GT catalytic mutation) (69) at chromosomal native
339 sites and *pbp2b*$^+$ or *rodA*$^+$ under the control of the zinc-inducible promoter (P_{Zn}) in an
340 ectopic site (Fig. 5*A*). The merodiploid strains were constructed and grown in the
341 presence of Zn inducer, which was removed to deplete the WT proteins (Fig. 5*B*).
342 Interestingly, we were able to construct a *rodA*(D283A)//P_{Zn}-*rodA*$^+$ strain, but we were
343 unable to construct a *pbp2b*(S391A)//P_{Zn}-*pbp2b*$^+$ strain in the presence of Zn inducer.
344 This result suggested that *pbp2b*(S391A) was dominant-negative to WT *pbp2b*$^+$. The
345 reason we were able to construct the *iht-pbp2b*(S391A)//P_{Zn}-*pbp2b*$^+$ merodiploid was the
346 low (≈15%) intrinsic expression of iHT-bPBP2b compared to WT bPBP2b (Fig. S4*B*).
347 Consistent with a dominant-negative effect, depletion of bPBP2b$^+$ in the *iht-*

348 *pbp2b*(S391A)//P_{Zn}-*pbp2b*$^+$ resulted in a more severe drop in OD_{620} than in Δ*pbp2b*//P_{Zn}-
349 *pbp2b*$^+$ (Fig. 5*B*), possibly due to the toxicity of uncrosslinked PG produced from GT
350 activity without TP activity (104). Western blot analysis confirmed that both iHT-
351 bPBP2b(S391A) and iHT-RodA(D283A) were expressed and stable relative to iHT-
352 bPBP2b$^+$ and iHT-RodA$^+$, respectively (Fig. S13*A*) and that bPBP2b$^+$ expressed from the
353 ectopic locus was fully depleted after 3h (Fig. S13*B*).

354 No midcell circumferential movement of iHT-bPBP2b(S391A) was detected in the
355 presence or absence of bPBP2b$^+$ (Fig. 5*C*; Movies S10 and S11). Instead, iHT-
356 bPBP2b(S391A) was static at midcell (Fig. 5*D*) or was detected diffusing over the body
357 of cells (Fig. 5*C*). Likewise, no midcell circumferential movement of iHT-RodA(D283A)
358 was detected in the absence of RodA$^+$ (Fig. 5*C* and Movie S12). Like iHT-
359 bPBP2b(S391A), iHT-RodA(D283A) was static at midcell (Fig. 5*D*) or diffusing over the
360 body of cells (Fig. 5*C*). Notably, both iHT-bPBP2b(S391A) and iHT-RodA(D283A) located
361 to midcell (Fig. 5*E*), indicating that catalytic activity was not required for normal
362 localization. From these combined results, we conclude that processive, circumferential
363 movement of the pneumococcal elongasome PG synthase is driven by PG synthesis, but
364 not by FtsZ treadmilling, even in predivisional cells.

365 **bPBP2b localization becomes diffuse and circumferential movement is lost**
366 **when MreC is depleted.** We reported previously that the pneumococcal PG elongasome
367 is assembled sequentially (19). RodZ directs localization of MreC, which then directs
368 localization of the bPBP2b:RodA synthase. In agreement with this conclusion, iHT-
369 bPBP2b localization became diffuse when MreC was depleted (Fig. 6*A*). In addition, there
370 was a large (≈30-fold) drop in the number of iHT-bPBP2b molecules moving

371 circumferentially when MreC was depleted (Fig. 6*B* and Movie S13). Growth curve
372 analysis confirmed reduced growth yield of cells depleted for MreC (Fig. S14*A*), and
373 western blots confirmed the presence of iHT-bPBP2b during MreC depletion (Fig. S14 *B*
374 and *C*). We conclude that MreC is required for proper midcell localization and for
375 elongasome PG synthesis by the bPBP2b:RodA synthase. This result is consistent with
376 the previous conclusion that MreC allosterically activates the GT/TP activity of
377 RodA:PBP2 in the PG elongasome of *E. coli* (16, 67, 105).

378 **bPBP2b and RodA require each other for localization.** We further tested whether
379 RodA was required for bPBP2b localization, and *vice versa*. Indeed, upon RodA
380 depletion, iHT-bPBP2b went from locating primarily to midcell to being distributed at
381 midcell and over the surface of rounded cells (Figs. 7*A* and S15*C*), indicative of loss of
382 peripheral PG synthesis (35, 75, 81). Additionally, a growth yield phenotype was observed
383 at 4 to 5 h into depletion (Fig. S15 *A* and *B*). Upon bPBP2b depletion to ≈6% of WT after
384 3 h (Fig. S13*B*), iHT-RodA also relocated primarily from midcell to being distributed at
385 midcell and over the surface of rounded cells, with a similar reduction in growth yield
386 (Figs. 7*B* and S15). Therefore, there is an interdependence for normal localization of
387 bPBP2b and RodA in the pneumococcal PG elongasome.

388 We next determined the dynamics of iHT-bPBP2b upon depletion of RodA or iHT-
389 RodA upon depletion of bPBP2b. In both cases, the motion distribution shifted from
390 primarily circumferential (≈59%) to diffusive (≈65%) movement (Fig. 7*C*; Movies S14 and
391 S15), where iHT-bPBP2b and likely iHT-RodA were underproduced in these stains (Figs.
392 1*B,* S7 and S13*B*). Remaining circumferential movement at the midcell (≈24% of
393 molecules) likely reflected bPBP2b:RodA complexes that assembled before depletion

394 occurred. Consistent with this interpretation, the velocity of circumferentially moving
395 proteins was unchanged by depletion of its cognate partner (Fig. 7 *D* and *E*). These data
396 support the idea that when bPBP2b or RodA is depleted, its unpaired cognate partner
397 stops elongation PG synthesis at midcell and is released to diffuse over the cell body.
398 Notably, released, unpaired iHT-bPBP2b or iHT-RodA did not move circumferentially at
399 an increased velocity, suggesting that FtsZ filament end-tracking does not occur for these
400 proteins (100).

401 **aPBP1a displays circumferential dynamics at midcell driven by PG synthesis**
402 **but is not persistently part of the elongasome.** Molecules of iHT-aPBP1a
403 unexpectedly displayed circumferential, as well as diffusive and static dynamics (Fig. 1 *A*
404 and *B*; Movies S16 to S18). Like iHT-bPBP2b and likely iHT-RodA, iHT-aPBP1a was
405 underproduced in the haploid strain and required ectopic expression to reach or surpass
406 WT levels (Fig. 1*B* and Fig. S5*B*). However, in contrast to core elongasome components,
407 the relative frequency of circumferentially moving iHT-aPBP1a molecules (≈10%) was
408 largely independent of protein expression level (Fig. 1*B*), and a high percentage (>60%)
409 of iHT-aPBP1a molecules moved diffusively, even at low expression levels (Fig. 1*B*; Fig.
410 S5*B*; Table S3).

411 The mean circumferential velocity of iHT-aPBP1a expressed near WT levels was ≈15
412 nm/s, which was similar to, if not somewhat faster than, that of iHT-bPBP2b, iHT-RodA,
413 and iHT-MreC (≈11 nm/s) (Figs. 1*A* and 3*A*). Strikingly, the mean circumferential duration
414 of iHT-aPBP1a molecules was ≈10 s, more than two-fold shorter than that of iHT-bPBP2b,
415 iHT-RodA, or iHT-MreC (≈23 s) (Fig. 1*A* and 3*B*). Altogether, these results indicate that
416 circumferential motion of aPBP1a is distinct from that of bPBP2b, RodA, and MreC,

417 suggesting that aPBP1a is not persistently part of the core elongasome complex,
418 although shorter interactions are still possible.

419 To confirm that circumferential movement of iHT-aPBP1a molecules depends on PG
420 synthesis, we constructed an *iht-pbp1a*(S370A)//P_{Zn}-*iht-pbp1a*(S370A) merodiploid strain
421 expressing catalytically inactive (TP null) iHT-aPBP1a(S370A) from both the native site
422 and ectopic locus (Table S1). The growth rate of the catalytically inactive iHT-
423 aPBP1a(S370A) merodiploid strain was reduced slightly (≈1.3-fold) when Zn inducer was
424 added to the growth medium (Fig. S16*A*), but protein expression and localization were
425 comparable to that of iHT-aPBP1a merodiploid strains (Fig. S16 *B* and *C*).
426 Circumferential, diffusive, and static molecules were sorted by cellular location into
427 midcell or locations other than midcell (non-midcell) (Fig. 8). Circumferential movement
428 of iHT-aPBP1a decreased substantially from a relative frequency of ≈21% for iHT-
429 aPBP1a to a marginal ≈3% for iHT-aPBP1a(S370A) at midcell, with the remainder of
430 midcell iHT-aPBP1a or iHT-aPBP1a(S370A) molecules static (Fig. 8, Movie S19).
431 Essentially no circumferentially moving molecules of iHT-aPBP1a or iHT-
432 aPBP1a(S370A) were detected outside of midcell (Fig. 8). A similar conclusion was
433 reached when data from Fig. 1*B* was sorted into midcell or non-midcell locations (Fig.
434 S17*A*). Since no PG synthesis was detectable by FDAA labeling away from the midcell
435 (Figs. 2 and S9), and nearly all aPBP1a molecules away from midcell were moving
436 diffusively (Figs. 8 and S17*A*), this further suggests that diffusively moving aPBP1a were
437 not actively synthesizing PG in exponentially growing cells. Taken together, these data
438 indicate that circumferentially moving iHT-aPBP1a molecules are actively synthesizing
439 PG, while inactive molecules are either static at midcell or moving diffusively throughout

440 the cell. A similar conclusion was reached for elongasome proteins iHT-bPBP2b, iHT-
441 RodA, and iHT-MreC (Figs. 1*B* and 2).

442 Other data were consistent with aPBP1a not being a constant component of the PG
443 elongasome. Notably, the velocity of iHT-aPBP1a in a merodiploid *iht-pbp1a*//P_{Zn}-*iht-*
444 *pbp1a* Δ*murZ* strain was similar to that of iHT-aPBP1a in a *murZ*$^+$ merodiploid strain (Fig.
445 S17*B*, Movie S20). Growth rate, protein amount, localization and relative frequency of
446 circumferential molecules of iHT-aPBP1a were also similar in the Δ*murZ* mutant and
447 *murZ*$^+$ strain (Figs. S16 and S17*C*). Therefore, unlike iHT-bPBP2b and iHT-RodA (Fig. 4
448 *C* and *D*), the circumferential velocity of iHT-aPBP1a was not decreased when PG
449 precursor amounts were reduced. In addition, we tested whether the relative frequency
450 of circumferential iHT-aPBP1a was changed in a *mpgA*(Y488D) Δ*pbp2b* mutant, which
451 lacks the core PG elongasome (80, 82). Reduced catalytic activity of MpgA(Y488D)
452 bypasses the requirement for the PG elongasome, but *mpgA*(Y488D) Δ*pbp2b* mutations
453 are synthetically lethal with Δ*pbp1a* (80), possibly indicating that aPBP1a can substitute
454 for the PG elongasome. Consistent with this notion, iHT-aPBP1a dynamics were the
455 same in a *mpgA*(Y488D) Δ*pbp2b* merodiploid strain as in a WT strain (Fig. S17*C*, Movie
456 S21).

457 **MpgA displays subdiffusive movement restricted to midcell.** We investigated the
458 dynamics of iHT-MpgA (previously MltG(*Spn*)) muramidase, which has been genetically
459 linked to elongasome PG synthesis (80, 82). At an image acquisition rate of 1 FPS, the
460 majority of iHT-MpgA molecules (≈87%) appeared to move diffusively, but seemed to be
461 constrained mainly to the midcell region of cells (Fig. 1*B* and Movie S22), consistent with
462 a previous report that sfGFP-MpgA localizes at midcell (34). The remaining ≈13% of iHT-

463 MpgA molecules were static at midcell (Fig. 1*B*). There was also a small fraction (<1%)
464 of iHT-MpgA molecules that appeared to display rapid (>50 nm/s) movement of very short
465 duration at midcell (Figs. 3*A*, 3*B*, and 9*A*). However, this motion was difficult to track and
466 at the limit of the criterion used for continuous motion (six consecutive frames).

467 Consequently, we increased the data acquisition rate to 10 FPS. At this higher rate,
468 iHT-MpgA did not exhibit the processive, unidirectional movement observed for the
469 elongasome components and for aPBP1a (Figs. 1*A* and 9*B*). Instead, iHT-MpgA moved
470 erratically, mainly in the midcell region (see below; Fig. 9*B* and Movie S23). Measured at
471 10 FPS, the mean velocity of iHT-MpgA moving in short, directional stretches was
472 relatively fast (≈327 nm/s) compared to circumferential movement of other proteins (<20
473 nm/s), but slower than diffusing molecules in non-midcell regions (>1,000 nm/s) (Fig. 9*C*).
474 These distinctive subdiffusive dynamics did not support persistent association of MpgA
475 with the PG elongasome or aPBP1a during PG synthesis.

476 Given these unusual dynamics, we confirmed the functionality of the iHT-MpgA fusion
477 construct. The growth and cell morphology of strains expressing iHT-MpgA were similar
478 to those of WT, and iHT-MpgA showed expected midcell localization (Fig. S2). A mutant
479 expressing partially active MpgA(Y488D) suppressed the essentiality of the
480 pneumococcal PG elongasome in transformation assays (80). However, the *iht-mpgA*
481 construct failed to suppress Δ*pbp2b*, Δ*rodA*, Δ*mreC*, or Δ*rodZ* in transformation assays
482 (Table S5), indicating iHT-MpgA possessed muramidase activity. Unlike Δ*mpgA* mutants,
483 which accumulate suppressor mutations that inactivate aPBP1a (80); no *pbp1a* mutations
484 were detected in the *iht-mpgA* fusion strain by Sanger DNA sequencing. These results

485 indicated that the iHT-MpgA fusion protein was substantially active and that its dynamics
486 accurately reflected those of WT MpgA.

487 **Core PG elongasome components, aPBP1a, and MpgA display different**
488 **diffusion patterns.** We next investigated diffusion dynamics by performing sm-TIRFm at
489 20 FPS (*Materials and Methods*). Individual molecular trajectories were tracked (Fig. 10*A*)
490 and used to calculate mean-squared displacements (MSD) and diffusion coefficients (Fig.
491 10*B*) (106, 107). Diffusion coefficients were between 0.040 and 0.055 $\mu m^2/s$, comparable
492 to values determined previously for PG synthesis proteins in *S. pneumoniae*, *E. coli* and
493 *B. subtilis* (56, 100, 108, 109). Consistent with sm-TIRFm imaging at 1 FPS (Fig. 1*B*),
494 single molecules displayed rapid diffusive motion in non-midcell regions and much slower,
495 processive motion at midcell, where static molecules were also observed (Fig. 10*A* and
496 Movies S24 to S30). MSD curves generated for diffusively moving molecules were not
497 linear and plateaued as time increased, with alpha values <1, which is indicative of some
498 form of subdiffusion (Fig. 10*B*). Subdiffusion is commonly due to diffusion within a
499 confined space, but can also be caused by membrane crowding or interactions with other
500 molecules (110). For bacterial membrane proteins, this confined space is often the
501 surface area of the cell membrane (110).

502 Single-molecule trajectories of diffusively moving PG elongasome core components
503 iHT-bPBP2b, iHT-RodA, and iHT-MreC covered most of the cell area, while non-diffusive
504 processive and static molecules located to midcell, where active PG synthesis occurred
505 (Fig. 10*A* and Movies S24 to S26), consistent with results acquired at 1 FPS (Fig. S8).
506 This suggests that the subdiffusive behavior of the core elongasome proteins was due to
507 confinement within the cell membrane. The diffusion coefficients of iHT-bPBP2b and iHT-

508 MreC were similar (≈0.046 μm^2/s), and the MSD curves of diffusively moving molecules
509 plateaued in the same range (≈0.07 μm^2), indicating that iHT-bPBP2b and iHT-MreC
510 molecules were confined to a similarly sized area (Fig. 10*B*) (111). By contrast, iHT-RodA
511 had a slightly higher diffusion coefficient (0.050 μm^2/s) with a higher MSD curve plateau
512 (≈0.08 μm^2). These data suggest that bPBP2b and MreC may diffuse as a complex
513 through the membrane separately from RodA. Additional experiments are needed to test
514 this idea.

515 Diffusively moving iHT-aPBP1a molecules had an even greater diffusion coefficient
516 (≈0.055 μm^2/s) than those of the core components of the PG elongasome (Fig. 10*B*). iHT-
517 aPBP1a molecules also had a higher plateau in MSD plots (≈0.1 μm^2), indicative of
518 diffusive movement that was observed over the whole cell (Fig. 10*A* and Movie S27).
519 Again, non-diffusive, processively moving and static iHT-aPBP1a molecules were mostly
520 confined to midcell (Fig. 10*A*), as was observed by sm-TIRFm at 1 FPS (Fig. 8 and S8).
521 Interestingly, we also observed some diffusive iHT-aPBP1a molecules that stopped
522 moving, paused for a short time (<1 s), and then resumed diffusive movement (Movie
523 S28). This pausing behavior was not readily detectable for diffusing components of the
524 PG elongasome. We conclude that diffusing aPBP1a molecules move differently from
525 components of the core PG elongasome in pneumococcal cells and that there is an
526 intermediate paused state during diffusion of aPBP1a.

527 Finally, diffusion analysis confirmed the unusual pattern of confined movement of iHT-
528 MpgA molecules at midcell. Unlike iHT-bPBP2b, iHT-RodA, iHT-MreC, and iHT-aPBP1a,
529 the majority of iHT-MpgA molecules did not diffuse over the whole cell but were largely
530 confined to midcell (Fig. 10*A* and Movie S29). This conclusion was further corroborated

531 by manually counting the location of iHT-MpgA tracks from data in Figure 10A. This
532 analysis showed that 74% (148/200) of the tracks of subdiffusive iHT-MpgA tracks were
533 located within 125 nm of midcell septa or equatorial rings. This confinement is likely
534 reflected by the low plateau (≈0.05 μm^2) in the MSD plot. In addition, the diffusion
535 coefficient (≈0.04 $\mu m^2/s$) of iHT-MpgA was considerably lower than those of the other
536 proteins that diffused over the body of cells (Fig. 10*B*), consistent with the sm-TIRFm
537 measurements at 10 FPS (Fig. 9). Similar to iHT-aPBP1a, iHT-MpgA subdiffusive
538 molecules were observed transitioning between diffusive motion and paused states
539 (Movie S30). Together, these results indicate that the confined, subdiffusive movement
540 of MpgA molecules is fundamentally different from that of components of the
541 pneumococcal core PG elongasome.
542

543 **DISCUSSION**

544 This paper shows that the core PG elongasome moves circumferentially around the
545 midcell of dividing *S. pneumoniae* cells (Fig. 1). The velocity of core elongasome
546 members bPBP2b, RodA, and MreC was statistically the same (≈11 nm/sec) (Fig. 3),
547 which is slightly slower than the velocity of the bPBP2x and FtsW (≈20 nm/sec)
548 components of the septal PG synthase (34). The processive motion of elongasome
549 members was driven by PG synthesis and was independent of FtsZ treadmilling (Fig. 4
550 and 5), and this motion was not dependent on stage of cell division (Fig. S10*B*). Strikingly,
551 the majority of bPBP2b or RodA molecules moved circumferentially in cells that severely
552 underproduced bPBP2b (≈15% of WT) or likely RodA (Fig. 1*B*). In contrast, in cells
553 expressing nearly WT protein levels, a minority of bPBP2b, RodA, and MreC molecules

554 either moved circumferentially and synthesized PG at midcell or exhibited nonmoving
555 static behavior at midcell (Fig. 1*B* and S8). The majority of core elongasome components
556 moved diffusively in the membrane over cell bodies, where PG synthesis was not
557 detected by FDAA labeling of exponentially growing cells (Fig. 2 and S9).

558 These observations indicate that pneumococcal elongation PG synthesis results from
559 processive, circumferential movement of PG elongasomes that are confined to a narrow
560 zone at midcell (Fig. 11). This pattern contrasts with the elongasome movement guided
561 by short MreB filaments and driven by PG synthesis that occurs over the body of many
562 rod-shaped bacteria (16). MreB-guided PG synthesis results in a dense mesh of
563 concentrically oriented PG glycan strands along the inner, sidewall surface of *B. subtilis*
564 cells (112). The circumferential movement of the pneumococcal PG elongasome
565 anticipates that peripheral PG glycan strands may likewise be concentrically aligned in *S.*
566 *pneumoniae* cells. These observations also indicate that in exponentially growing WT
567 cells, the core elongasome components are present in excess, with only a minority of
568 bPBP2b, RodA, and MreC engaged in active PG synthesis at midcell rings (Fig. 2 and
569 S9).

570 The results presented here further raise the issue of what directs circumferential
571 movement of elongasome components in tracks at midcell. The velocity of elongasome
572 components was not changed when treadmilling was greatly impeded in an *ftsZ*(GTPase)
573 mutant (Fig. 4*A*). Independence of FtsZ treadmilling fits the observation that FtsZ was not
574 detected in the outer midcell ring where peripheral PG synthesis occurs later in division
575 (Fig. S1*B*) (32). The similar velocity of MreC in predivisional cells when elongasomes are
576 still located in the FtsZ-ring as in later-divisional cells when the elongasome is in outer

577 midcell ring (Fig. S10*B*) is also consistent with independence of FtsZ treadmilling. It was
578 recently suggested that FtsZ treadmilling may play a role in determining the speed of the
579 septal PG synthase in *B. subtilis* (56). This conclusion was based on a modest decrease
580 (≈40%) in bPBP2 speed when FtsZ treadmilling rate was moderately or greatly reduced
581 (56). However, other indirect mechanisms could contribute to decreased bPBP2 speed,
582 such as a possible decrease in Lipid II amount when FtsZ treadmilling is decreased. In
583 pneumococcus, severely decreased FtsZ treadmilling speed had a marginal (≈17%) (34)
584 or no effect (Fig. 4*A*) on the septal or elongasome PG synthase speed, respectively. In
585 addition, when RodA or bPBP2b was depleted, no unassociated bPBP2b or RodA was
586 detected being driven at the rate of treadmilling FtsZ (≈34 nm/sec; Fig 7 *D* and *E*), as
587 occurs for components of the septal PG synthase of *E. coli* (100). Thus, all evidence
588 supports the conclusion that the movement and speed of the septal and elongasome PG
589 synthases are driven by PG synthesis, independent of FtsZ treadmilling, in WT *S.*
590 *pneumoniae* cells.

591 It remains unknown what determines the tracks for the movement of the
592 pneumococcal septal or elongasome PG synthases in the inner and outer midcell rings,
593 respectively (Fig. S1). The muropeptide-crosslinked PG glycan strands to which new PG
594 is added may provide a rigid structure that directs processive PG synthesis in a linear
595 direction. Moreover, there appears to be a limited number of available sites in midcell
596 rings for septal and elongasome PG synthases to load and synthesize PG. As noted
597 above, only a minority of elongasome components are engaged in PG synthesis in WT
598 cells (Fig. 1*B*, 2, and 11). However, when the cellular amount of bPBP2b was reduced to
599 ≈15% of the WT level, the majority of bPBP2b molecules moved processively to

synthesize PG (Fig. 1*B*), consistent with a limited number of spots on rings for active PG synthase complexes. Interestingly, ≈26% of circumferentially moving bPBP2b or MreC molecules reversed direction within the timeframe of these experiments. Direction reversal was also reported for processively moving members of the septal PG synthases of *S. aureus* (55) and *B. subtilis* (113). This directional transitioning may be indicative of PG synthase complexes stopping and reinitiating synthesis of a new glycan strand in the opposite direction (55, 113).

We also observed nonmoving, static molecules of bPBP2b, RodA, and MreC expressed at WT concentrations, primarily at midcell and to a lesser (≈5-fold) extent elsewhere in cells (Fig. 1*B* and S8). When elongasome PG synthesis was halted by expression of catalytically inactive proteins, circumferential movement also stopped and molecules became static (Fig. 5*C* and 5*D*; Fig. 8) (69). To our knowledge, there is no direct evidence that PBPs static for several seconds are actively synthesizing PG, as suggested for aPBPs in *E. coli* (71, 74). To the contrary, when PG synthases stop synthesis, they stop moving (Fig. 5 *C* and *D*; Fig. 8) (34, 55, 56, 114). Therefore, we think it more likely that static PG synthases at midcell in WT cells may be incompletely assembled complexes or complexes waiting to assume an available site for PG synthesis. Consistent with this idea, we observed transitions of MreC molecules from the processive to static states (<5%), and *vice versa* (<1%). Outside of midcell, diffusion analysis showed that inactive bPBP2b and MreC may diffuse together as a complex over the cell body, while RodA diffuses separately (Fig. 10*B*). The mechanisms that arrange and limit the number of active pneumococcal PG elongasomes remain to be determined.

622 The processive movement of pneumococcal Class A aPBP1a strikingly contrasts with
623 the diffusive motion for Class A PBPs reported previously in *E. coli* and *B. subtilis* (71,
624 74). Earlier IFM studies colocalized aPBP1a with elongasome components bPBP2b and
625 MreC (35). Instead of diffusive motion, aPBP1a molecules at midcell moved
626 circumferentially or were static (Fig. 8 and S17), and processive movement was abolished
627 in a *pbp1a*(TP) mutant (Fig. 8). Processively moving aPBP1a also reversed direction
628 infrequently (<9%). However, several results indicate that aPBP1a is not a persistent
629 member of the core PG elongasome. The duration of aPBP1a processive motion was
630 considerably shorter (≈10 s) than that of the PG elongasome components (≈23 s) (Fig.
631 3*B*). In addition, the relative frequency of circumferential motion of aPBP1a was
632 unchanged in a suppressed Δ*pbp2b mpgA*(Y488D) mutant that lacks an intact PG
633 elongasome (Fig. S17*C*). Like iHT-bPBP2b, iHT-aPBP1a was underproduced (10% of
634 WT) when expressed from its native chromosomal locus (Figs. 1*B* and S5*B*). But, unlike
635 iHT-bPBP2b, circumferentially moving aPBP1a was not the majority species at the low
636 expression level (Fig. 1*B*). In addition, unlike bPBP2b and RodA, aPBP1a processive
637 motion was not decreased in a Δ*murZ* mutant (Fig. S17 *B* and *C*), which may reflect a
638 different kinetic dependence for Lipid II substrate. Outside of midcell, aPBP1a moved
639 diffusively in the membrane over the whole length of cells (Figs. 8 and 10*A*). Together,
640 these results indicate that aPBP1a is not a persistent member of the pneumococcal core
641 PG elongasome (85), although shorter or transient interactions are possible (Fig. 11).

642 aPBPs have been proposed to play roles in normal PG synthesis and in repair of
643 damaged PG (1, 39, 73, 115). In rod-shaped bacteria, it was postulated that when
644 diffusing aPBPs encounter damaged PG, they cease moving and become static for

645 relatively long times (≈5 s) (71, 74). For reasons discussed above, long static PG
646 synthases may not be synthesizing PG. We also detected another aPBP1a motion away
647 from midcell in exponentially growing cells. Diffusing aPBP1a molecules infrequently
648 paused for short (<1 s) intervals, before resuming diffusive motion (Movie S28). It remains
649 to be determined whether static or paused aPBP1a molecules are repairing damaged PG
650 in *S. pneumoniae* cells.

651 In Gram-positive bacteria, the PG in the septal annular disk has a core of concentric
652 ordered PG glycan strands covered by a dense mesh of randomly oriented PG strands
653 that face the cell membrane (112). It has been postulated that aPBPs may synthesize this
654 layer of randomly oriented, inner-facing PG strands (39), although remodeling by PG
655 hydrolases followed by resynthesis could potentially contribute to this disordered pattern.
656 Circumferential, processive movement suggests that aPBP1a synthesis may result in
657 concentric, ordered PG glycan strands, rather than randomly oriented strands. Glycan
658 strands synthesized by the shorter tracks of aPBP1a motion are presumably shorter than
659 those synthesized by the more processive core PG elongasome. These shorter strands
660 may be remodeled and crosslinked into the longer strands to provide additional strength
661 to the peripheral PG layer. The dynamics of the other pneumococcal Class A PBPs,
662 aPBP2a and aPBP1b, remains to be determined. The circumferential movement of an
663 aPBP potentially has another implication to bacteria that elongate only from their poles,
664 such as *Rhizobiales* species, including *Agrobacterium tumefaciens* (116, 117). Polar
665 elongasome complexes in these bacteria lack bPBP:SEDS PG synthases, and PG
666 elongation is carried out only by a single essential aPBP (116, 117), which may move
667 circumferentially during PG elongation.

668 Finally, the subdiffusional, confined motion of the MpgA muramidase at midcell was
669 unexpected. IFM showed that MpgA (formerly MltG(*Spn*)), like aPBP1a, colocalized with
670 MreC to the outer ring in later-divisional cells (80). MpgA is an essential muramidase that
671 cleaves newly synthesized PG glycan chains 7 disaccharides from the undecaprenol
672 membrane anchor (82). A LysM domain in MpgA correctly places the cleavage point in
673 the glycan chain. Therefore, MpgA is thought to act as a PG release factor that frees
674 newly synthesized PG for crosslinking into existing PG (82). Instead of moving
675 circumferentially, most MpgA molecules moved at subdiffusion speeds (≈300 nm/sec)
676 that were slower than that of freely diffusing MpgA (>1,000 nm/sec). However, instead of
677 moving over the whole body of cells, MpgA molecules were largely confined to regions of
678 PG synthesis at midcell (Figs. 1*B* and 10*A*). Therefore, MpgA functions separately from
679 the core PG elongasome and from aPBP1a (Fig. 11). Only a fraction (≈13%) of MpgA
680 molecules were static, and we detected subdiffusing MpgA molecules that paused (<1 s)
681 and then resumed movement (Movie S30), similar to aPBP1a. Whether static or paused
682 MpgA are carrying out PG strand cleavage requires further study. Likewise, proteins that
683 interact with and regulate MpgA activity (118) and the mechanism that confines MpgA
684 movement to midcell await discovery.
685

686 **MATERIALS AND METHODS**

687 Bacterial strains used were unencapsulated (Δ*cps*) derivatives of *Streptococcus*
688 *pneumoniae* (*Spn*) serotype 2 strain D39W and are listed in Table S1. IU1945 and IU1824
689 were used as parent strains (Table S1). Detailed methods are described in *SI Appendix,*
690 *Materials and Methods*, including: bacterial strain construction and growth conditions;

691 ectopic expression and depletion conditions; cell labeling with HaloTag ligand; 2D-
692 epifluorescence microscopy and analysis; sm-TIRFm sample preparation; sm-TIRFm
693 imaging; sm-TIRFm image analysis; single-molecule tracking and diffusion analysis; 3D-
694 structured illumination microscopy and analysis; quantitative western blotting;
695 transformation assay.
696

697 **ACKNOWLEDGEMENTS**

698 We thank laboratory members and Jie Xiao (Johns Hopkins) for discussions about this
699 work; John D. Richardson and Ziyun A. Ye for technical assistance with some
700 experiments, Jim Powers (Indiana University Bloomington) for advice about light
701 microscopy; Mike VanNieuwenhze (Indiana University Bloomington) for FDAA reagents;
702 Luke Lavis (Janelia Lab) for Fluor JF549; Reinhold Brückner, and Regine Hakenbeck
703 (Kaiserlautern University) for anti-bPBP2x antibody; and Suzanne Walker and David Z.
704 Rudner (Harvard Medical School) for antibodies against pneumococcal PG synthesis
705 proteins. This work was supported by NIH brant R35GM131767 (to MEW), NSF grant
706 MCB1027504 (to SLS); NIH grant RO1AI148752 (to Suzanne Walker); NIH grant T32
707 GM109825 (to AJP); NIH grant F31AI138430 (to MML); NIH grants T32 GM007753 and
708 F30 AI156972 (to JEP), and NIH equipment grant S10OD024988 to the Indiana University
709 Bloomington (IUB) Light Microscopy Imaging Center.
710

711 **CONFLICT OF INTEREST**

712 The authors declare that they have no conflicts of interests.
713

AUTHOR CONTRIBUTIONS

AJP, MML, KEB, SLS, and MEW contributed to the conception or design of this study. AJP, MML, KEB, MAT, JEP SLS, HCTT, and MEW contributed to the acquisition, analysis, and interpretation of the data. KEB, HCTT, and MEW contributed to the writing of the manuscript with input from the other authors.

DATA AVAILABILITY

The data that support the findings of this study are presented in the paper, including the Supplemental Information and Appendix A.

ORCID

Amilcar J. Perez https://orcid.org/0000-0001-6729-7564

Melissa M. Lamanna https://orcid.org/0000-0002-6535-7903

Kevin E. Bruce https://orcid.org/0009-0005-3300-8863

Julia E. Page https://orcid.org/0000-0002-9884-2382

Sidney L. Shaw https://orcid.org/0000-0001-9195-6128

Ho-Ching T. Tsui https://orcid.org/0000-0003-0849-874X

Malcolm E. Winkler https://orcid.org/0000-0002-1482-2588

REFERENCES

1. E. A. Mueller, P. A. Levin, Bacterial Cell Wall Quality Control during Environmental Stress. *mBio* **11** (2020).
2. M. Rajagopal, S. Walker, Envelope Structures of Gram-Positive Bacteria. *Curr Top Microbiol Immunol* **404**, 1-44 (2017).
3. E. R. Rojas, The Mechanical Properties of Bacteria and Why they Matter. *Adv Exp Med Biol* **1267**, 1-14 (2020).

4. W. Vollmer, O. Massidda, A. Tomasz, The Cell Wall of Streptococcus pneumoniae. *Microbiol Spectr* **7** (2019).
5. K. D. Young, Bacterial shape: two-dimensional questions and possibilities. *Annu Rev Microbiol* **64**, 223-240 (2010).
6. K. Bush, P. A. Bradford, Interplay between beta-lactamases and new beta-lactamase inhibitors. *Nat Rev Microbiol* **17**, 295-306 (2019).
7. T. den Blaauwen, J. M. Andreu, O. Monasterio, Bacterial cell division proteins as antibiotic targets. *Bioorg Chem* **55**, 27-38 (2014).
8. K. Lewis, The Science of Antibiotic Discovery. *Cell* **181**, 29-45 (2020).
9. L. L. Ling *et al.*, A new antibiotic kills pathogens without detectable resistance. *Nature* **517**, 455-459 (2015).
10. L. T. Sham, H. C. Tsui, A. D. Land, S. M. Barendt, M. E. Winkler, Recent advances in pneumococcal peptidoglycan biosynthesis suggest new vaccine and antimicrobial targets. *Curr Opin Microbiol* **15**, 194-203 (2012).
11. J. Zhou *et al.*, Breaking down the cell wall: Still an attractive antibacterial strategy. *Front Microbiol* **13**, 952633 (2022).
12. S. Booth, R. J. Lewis, Structural basis for the coordination of cell division with the synthesis of the bacterial cell envelope. *Protein Sci* **28**, 2042-2054 (2019).
13. A. J. F. Egan, J. Errington, W. Vollmer, Regulation of peptidoglycan synthesis and remodelling. *Nat Rev Microbiol* **18**, 446-460 (2020).
14. S. Garde, P. K. Chodisetti, M. Reddy, Peptidoglycan: Structure, Synthesis, and Regulation. *EcoSal Plus* **9** (2021).
15. S. Kumar, A. Mollo, D. Kahne, N. Ruiz, The Bacterial Cell Wall: From Lipid II Flipping to Polymerization. *Chem Rev* **122**, 8884-8910 (2022).
16. P. D. A. Rohs, T. G. Bernhardt, Growth and Division of the Peptidoglycan Matrix. *Annu Rev Microbiol* **75**, 315-336 (2021).
17. C. Billaudeau *et al.*, Contrasting mechanisms of growth in two model rod-shaped bacteria. *Nat Commun* **8**, 15370 (2017).
18. P. J. Eswara, K. S. Ramamurthi, Bacterial Cell Division: Nonmodels Poised to Take the Spotlight. *Annu Rev Microbiol* **71**, 393-411 (2017).
19. M. M. Lamanna *et al.*, Roles of RodZ and class A PBP1b in the assembly and regulation of the peripheral peptidoglycan elongasome in ovoid-shaped cells of Streptococcus pneumoniae D39. *Mol Microbiol* **118**, 336-368 (2022).
20. S. P. Ouellette, J. Lee, J. V. Cox, Division without Binary Fission: Cell Division in the FtsZ-Less Chlamydia. *J Bacteriol* **202** (2020).
21. A. R. Pereira *et al.*, FtsZ-Dependent Elongation of a Coccoid Bacterium. *mBio* **7** (2016).
22. M. G. Pinho, M. Kjos, J. W. Veening, How to get (a)round: mechanisms controlling growth and division of coccoid bacteria. *Nat Rev Microbiol* **11**, 601-614 (2013).
23. A. M. Randich, Y. V. Brun, Molecular mechanisms for the evolution of bacterial morphologies and growth modes. *Front Microbiol* **6**, 580 (2015).
24. N. S. Briggs, K. E. Bruce, S. Naskar, M. E. Winkler, D. I. Roper, The Pneumococcal Divisome: Dynamic Control of Streptococcus pneumoniae Cell Division. *Front Microbiol* **12**, 737396 (2021).

25. O. Massidda, L. Novakova, W. Vollmer, From models to pathogens: how much have we learned about Streptococcus pneumoniae cell division? *Environ Microbiol* **15**, 3133-3157 (2013).
26. M. J. Cox, N. Loman, D. Bogaert, J. O'Grady, Co-infections: potentially lethal and unexplored in COVID-19. *Lancet Microbe* **1**, e11 (2020).
27. V. Sender, K. Hentrich, B. Henriques-Normark, Virus-Induced Changes of the Respiratory Tract Environment Promote Secondary Infections With Streptococcus pneumoniae. *Front Cell Infect Microbiol* **11**, 643326 (2021).
28. J. N. Weiser, D. M. Ferreira, J. C. Paton, Streptococcus pneumoniae: transmission, colonization and invasion. *Nat Rev Microbiol* **16**, 355-367 (2018).
29. CDC (2019) Antibiotic resistance threats in the United States, 2019. in *AR Threats Rep., U.S. Dep. Health Hum. Serv., Cent. Dis. Control Prev.* (AR Threats Report, U.S.A. Dept Health and Human Services, Center for Disease Control and Prevention, Atlanta, GA).
30. P. S. Gibson, J. W. Veening, Gaps in the wall: understanding cell wall biology to tackle amoxicillin resistance in Streptococcus pneumoniae. *Curr Opin Microbiol* **72**, 102261 (2023).
31. WHO (2017) List of bacteria for which new antibiotics are urgently needed. (World Health Organization, Geneva, Switzerland).
32. A. J. Perez *et al.*, Organization of peptidoglycan synthesis in nodes and separate rings at different stages of cell division of Streptococcus pneumoniae. *Mol Microbiol* **115**, 1152-1169 (2021).
33. J. Trouve *et al.*, Nanoscale dynamics of peptidoglycan assembly during the cell cycle of Streptococcus pneumoniae. *Curr Biol* **31**, 2844-2856 e2846 (2021).
34. A. J. Perez *et al.*, Movement dynamics of divisome proteins and PBP2x:FtsW in cells of Streptococcus pneumoniae. *Proc Natl Acad Sci U S A* **116**, 3211-3220 (2019).
35. H. T. Tsui *et al.*, Pbp2x localizes separately from Pbp2b and other peptidoglycan synthesis proteins during later stages of cell division of Streptococcus pneumoniae D39. *Mol Microbiol* **94**, 21-40 (2014).
36. J. Errington, L. J. Wu, Cell Cycle Machinery in Bacillus subtilis. *Subcell Biochem* **84**, 67-101 (2017).
37. V. A. Lund *et al.*, Molecular coordination of Staphylococcus aureus cell division. *Elife* **7** (2018).
38. B. M. Saraiva *et al.*, Reassessment of the distinctive geometry of Staphylococcus aureus cell division. *Nat Commun* **11**, 4097 (2020).
39. D. Straume, K. W. Piechowiak, M. Kjos, L. S. Havarstein, Class A PBPs: It is time to rethink traditional paradigms. *Mol Microbiol* **116**, 41-52 (2021).
40. R. Wheeler, S. Mesnage, I. G. Boneca, J. K. Hobbs, S. J. Foster, Super-resolution microscopy reveals cell wall dynamics and peptidoglycan architecture in ovococcal bacteria. *Mol Microbiol* **82**, 1096-1109 (2011).
41. A. J. Perez *et al.*, FtsZ-Ring Regulation and Cell Division Are Mediated by Essential EzrA and Accessory Proteins ZapA and ZapJ in Streptococcus pneumoniae. *Front Microbiol* **12**, 780864 (2021).
42. A. Fleurie *et al.*, MapZ marks the division sites and positions FtsZ rings in Streptococcus pneumoniae. *Nature* **516**, 259-262 (2014).

43. N. Holeckova *et al.*, LocZ is a new cell division protein involved in proper septum placement in Streptococcus pneumoniae. *mBio* **6**, e01700-01714 (2014).
44. V. W. Rowlett, W. Margolin, The Min system and other nucleoid-independent regulators of Z ring positioning. *Front Microbiol* **6**, 478 (2015).
45. L. J. Wu, J. Errington, Nucleoid occlusion and bacterial cell division. *Nat Rev Microbiol* **10**, 8-12 (2011).
46. A. D. Land *et al.*, Requirement of essential Pbp2x and GpsB for septal ring closure in Streptococcus pneumoniae D39. *Mol Microbiol* **90**, 939-955 (2013).
47. R. van Raaphorst, M. Kjos, J. W. Veening, Chromosome segregation drives division site selection in Streptococcus pneumoniae. *Proc Natl Acad Sci U S A* **114**, E5959-E5968 (2017).
48. M. Jacq *et al.*, Remodeling of the Z-Ring Nanostructure during the Streptococcus pneumoniae Cell Cycle Revealed by Photoactivated Localization Microscopy. *mBio* **6** (2015).
49. A. Mura *et al.*, Roles of the Essential Protein FtsA in Cell Growth and Division in Streptococcus pneumoniae. *J Bacteriol* **199** (2017).
50. P. A. Levin, A. Janakiraman, Localization, Assembly, and Activation of the Escherichia coli Cell Division Machinery. *EcoSal Plus* **9**, eESP00222021 (2021).
51. C. R. Mahone, E. D. Goley, Bacterial cell division at a glance. *J Cell Sci* **133** (2020).
52. L. M. Y. Mertens, T. den Blaauwen, Optimising expression of the large dynamic range FRET pair mNeonGreen and superfolder mTurquoise2(ox) for use in the Escherichia coli cytoplasm. *Sci Rep* **12**, 17977 (2022).
53. A. W. Bisson-Filho *et al.*, Treadmilling by FtsZ filaments drives peptidoglycan synthesis and bacterial cell division. *Science* **355**, 739-743 (2017).
54. X. Yang *et al.*, A two-track model for the spatiotemporal coordination of bacterial septal cell wall synthesis revealed by single-molecule imaging of FtsW. *Nat Microbiol* **6**, 584-593 (2021).
55. S. Schäper *et al.*, Processive movement of Staphylococcus aureus essential septal peptidoglycan synthases is independent of FtsZ treadmilling and drives cell constriction. *bioRxiv* 10.1101/2023.06.29.547026 (2023).
56. K. D. Whitley, J. Grimshaw, E. Karinou, P. J. Stansfeld, S. Holden, A one-track model for spatiotemporal coordination of Bacillus subtilis septal cell wall synthesis. *bioRxiv* 10.1101/2023.06.29.547024, 2023.2006.2029.547024 (2023).
57. J. Dominguez-Escobar *et al.*, Processive movement of MreB-associated cell wall biosynthetic complexes in bacteria. *Science* **333**, 225-228 (2011).
58. E. C. Garner *et al.*, Coupled, circumferential motions of the cell wall synthesis machinery and MreB filaments in B. subtilis. *Science* **333**, 222-225 (2011).
59. S. van Teeffelen *et al.*, The bacterial actin MreB rotates, and rotation depends on cell-wall assembly. *Proc Natl Acad Sci U S A* **108**, 15822-15827 (2011).
60. B. P. Bratton, J. W. Shaevitz, Z. Gitai, R. M. Morgenstein, MreB polymers and curvature localization are enhanced by RodZ and predict E. coli's cylindrical uniformity. *Nat Commun* **9**, 2797 (2018).
61. S. Hussain *et al.*, MreB filaments align along greatest principal membrane curvature to orient cell wall synthesis. *Elife* **7**, e32471 (2018).

873 62. R. M. Morgenstein *et al.*, RodZ links MreB to cell wall synthesis to mediate MreB
874 rotation and robust morphogenesis. *Proc Natl Acad Sci U S A* **112**, 12510-12515
875 (2015).
876 63. R. Ago, D. Shiomi, RodZ: a key-player in cell elongation and cell division in
877 Escherichia coli. *AIMS Microbiol* **5**, 358-367 (2019).
878 64. F. O. Bendezu, C. A. Hale, T. G. Bernhardt, P. A. de Boer, RodZ (YfgA) is required
879 for proper assembly of the MreB actin cytoskeleton and cell shape in E. coli. *EMBO*
880 *J* **28**, 193-204 (2009).
881 65. F. van den Ent, C. M. Johnson, L. Persons, P. de Boer, J. Lowe, Bacterial actin MreB
882 assembles in complex with cell shape protein RodZ. *EMBO J* **29**, 1081-1090
883 (2010).
884 66. A. J. Meeske *et al.*, SEDS proteins are a widespread family of bacterial cell wall
885 polymerases. *Nature* **537**, 634-638 (2016).
886 67. P. D. A. Rohs *et al.*, A central role for PBP2 in the activation of peptidoglycan
887 polymerization by the bacterial cell elongation machinery. *PLoS Genet* **14**,
888 e1007726 (2018).
889 68. P. D. A. Rohs *et al.*, Identification of potential regulatory domains within the MreC and
890 MreD components of the cell elongation machinery. *J Bacteriol* 10.1128/JB.00493-
891 20 (2021).
892 69. M. Sjodt *et al.*, Structure of the peptidoglycan polymerase RodA resolved by
893 evolutionary coupling analysis. *Nature* **556**, 118-121 (2018).
894 70. M. Sjodt *et al.*, Structural coordination of polymerization and crosslinking by a SEDS-
895 bPBP peptidoglycan synthase complex. *Nat Microbiol* **5**, 813-820 (2020).
896 71. H. Cho *et al.*, Bacterial cell wall biogenesis is mediated by SEDS and PBP polymerase
897 families functioning semi-autonomously. *Nat Microbiol* **1**, 16172 (2016).
898 72. M. F. Dion *et al.*, Bacillus subtilis cell diameter is determined by the opposing actions
899 of two distinct cell wall synthetic systems. *Nat Microbiol* **4**, 1294-1305 (2019).
900 73. M. Pazos, W. Vollmer, Regulation and function of class A Penicillin-binding proteins.
901 *Curr Opin Microbiol* **60**, 80-87 (2021).
902 74. A. Vigouroux *et al.*, Class-A penicillin binding proteins do not contribute to cell shape
903 but repair cell-wall defects. *Elife* **9**, e51998 (2020).
904 75. K. H. Berg, G. A. Stamsas, D. Straume, L. S. Havarstein, Effects of low PBP2b levels
905 on cell morphology and peptidoglycan composition in Streptococcus pneumoniae
906 R6. *J Bacteriol* **195**, 4342-4354 (2013).
907 76. J. Philippe, T. Vernet, A. Zapun, The elongation of ovococci. *Microb Drug Resist* **20**,
908 215-221 (2014).
909 77. G. A. Stamsas *et al.*, Identification of EloR (Spr1851) as a regulator of cell elongation
910 in Streptococcus pneumoniae. *Mol Microbiol* **105**, 954-967 (2017).
911 78. D. Straume, G. A. Stamsas, K. H. Berg, Z. Salehian, L. S. Havarstein, Identification of
912 pneumococcal proteins that are functionally linked to penicillin-binding protein 2b
913 (PBP2b). *Mol Microbiol* **103**, 99-116 (2017).
914 79. J. J. Zheng, A. J. Perez, H. T. Tsui, O. Massidda, M. E. Winkler, Absence of the KhpA
915 and KhpB (JAG/EloR) RNA-binding proteins suppresses the requirement for
916 PBP2b by overproduction of FtsA in Streptococcus pneumoniae D39. *Mol*
917 *Microbiol* **106**, 793-814 (2017).

80. H. C. Tsui *et al.*, Suppression of a deletion mutation in the gene encoding essential PBP2b reveals a new lytic transglycosylase involved in peripheral peptidoglycan synthesis in Streptococcus pneumoniae D39. *Mol Microbiol* **100**, 1039-1065 (2016).
81. A. D. Land, M. E. Winkler, The requirement for pneumococcal MreC and MreD is relieved by inactivation of the gene encoding PBP1a. *J Bacteriol* **193**, 4166-4179 (2011).
82. A. Taguchi, J. E. Page, H. T. Tsui, M. E. Winkler, S. Walker, Biochemical reconstitution defines new functions for membrane-bound glycosidases in assembly of the bacterial cell wall. *Proc Natl Acad Sci U S A* **118** (2021).
83. A. K. Fenton, L. El Mortaji, D. T. Lau, D. Z. Rudner, T. G. Bernhardt, CozE is a member of the MreCD complex that directs cell elongation in Streptococcus pneumoniae. *Nat Microbiol* **2**, 16237 (2016).
84. M. M. Lamanna, A. T. Maurelli, What Is Motion? Recent Advances in the Study of Molecular Movement Patterns of the Peptidoglycan Synthesis Machines. *J Bacteriol* **204**, e0059821 (2022).
85. C. Lenoir *et al.*, The morphogenic protein CopD controls the spatio-temporal dynamics of PBP1a and PBP2b in Streptococcus pneumoniae. *mBio* **14**, e0141123 (2023).
86. S. G. Bartual *et al.*, Structural basis of PcsB-mediated cell separation in Streptococcus pneumoniae. *Nature communications* **5**, 3842 (2014).
87. B. E. Rued *et al.*, Structure of the Large Extracellular Loop of FtsX and Its Interaction with the Essential Peptidoglycan Hydrolase PcsB in Streptococcus pneumoniae. *mBio* **10** (2019).
88. L. T. Sham, S. M. Barendt, K. E. Kopecky, M. E. Winkler, Essential PcsB putative peptidoglycan hydrolase interacts with the essential FtsXSpn cell division protein in Streptococcus pneumoniae D39. *Proc Natl Acad Sci U S A* **108**, E1061-1069 (2011).
89. L. T. Sham, K. R. Jensen, K. E. Bruce, M. E. Winkler, Involvement of FtsE ATPase and FtsX extracellular loops 1 and 2 in FtsEX-PcsB complex function in cell division of Streptococcus pneumoniae D39. *mBio* **4** (2013).
90. P. Domínguez-Cuevas, I. Porcelli, R. A. Daniel, J. Errington, Differentiated roles for MreB-actin isologues and autolytic enzymes in Bacillus subtilis morphogenesis. *Mol Microbiol* **89**, 1084-1098 (2013).
91. J. Meisner *et al.*, FtsEX is required for CwlO peptidoglycan hydrolase activity during cell wall elongation in Bacillus subtilis. *Mol Microbiol* **89**, 1069-1083 (2013).
92. M. J. Catalão, J. Figueiredo, M. X. Henriques, J. P. Gomes, S. R. Filipe, Optimization of fluorescent tools for cell biology studies in Gram-positive bacteria. *PLoS One* **9**, e113796 (2014).
93. J. B. Grimm *et al.*, A general method to improve fluorophores for live-cell and single-molecule microscopy. *Nat Methods* **12**, 244-250, 243 p following 250 (2015).
94. M. X. Henriques, M. J. Catalão, J. Figueiredo, J. P. Gomes, S. R. Filipe, Construction of improved tools for protein localization studies in Streptococcus pneumoniae. *PLoS One* **8**, e55049 (2013).
95. G. V. Los *et al.*, HaloTag: a novel protein labeling technology for cell imaging and protein analysis. *ACS Chem Biol* **3**, 373-382 (2008).

963 96. K. Peters *et al.*, Streptococcus pneumoniae PBP2x mid-cell localization requires the
964 C-terminal PASTA domains and is essential for cell shape maintenance. *Mol*
965 *Microbiol* **92**, 733-755 (2014).
966 97. N. Ke, D. Landgraf, J. Paulsson, M. Berkmen, Visualization of Periplasmic and
967 Cytoplasmic Proteins with a Self-Labeling Protein Tag. *J Bacteriol* **198**, 1035-1043
968 (2016).
969 98. A. Eberhardt, L. J. Wu, J. Errington, W. Vollmer, J. W. Veening, Cellular localization
970 of choline-utilization proteins in Streptococcus pneumoniae using novel
971 fluorescent reporter systems. *Mol Microbiol* **74**, 395-408 (2009).
972 99. F. E. Jacobsen, K. M. Kazmierczak, J. P. Lisher, M. E. Winkler, D. P. Giedroc,
973 Interplay between manganese and zinc homeostasis in the human pathogen
974 Streptococcus pneumoniae. *Metallomics : integrated biometal science* **3**, 38-41
975 (2011).
976 100. J. W. McCausland *et al.*, Treadmilling FtsZ polymers drive the directional
977 movement of sPG-synthesis enzymes via a Brownian ratchet mechanism. *Nat*
978 *Commun* **12**, 609 (2021).
979 101. H. T. Tsui *et al.*, Negative regulation of MurZ and MurA underlies the essentiality
980 of GpsB- and StkP-mediated protein phosphorylation in Streptococcus
981 pneumoniae D39. *Mol Microbiol* **120**, 351-383 (2023).
982 102. O. Kocaoglu, H. C. Tsui, M. E. Winkler, E. E. Carlson, Profiling of β-lactam
983 selectivity for penicillin-binding proteins in Streptococcus pneumoniae D39.
984 *Antimicrob Agents Chemother* **59**, 3548-3555 (2015).
985 103. K. H. Berg, D. Straume, L. S. Havarstein, The function of the transmembrane and
986 cytoplasmic domains of pneumococcal penicillin-binding proteins 2x and 2b
987 extends beyond that of simple anchoring devices. *Microbiology (Reading)* **160**,
988 1585-1598 (2014).
989 104. H. Cho, T. Uehara, T. G. Bernhardt, Beta-lactam antibiotics induce a lethal
990 malfunctioning of the bacterial cell wall synthesis machinery. *Cell* **159**, 1300-1311
991 (2014).
992 105. I. Shlosman *et al.*, Allosteric activation of cell wall synthesis during bacterial
993 growth. *Nat Commun* **14**, 3439 (2023).
994 106. N. Tarantino *et al.*, TNF and IL-1 exhibit distinct ubiquitin requirements for inducing
995 NEMO-IKK supramolecular structures. *J Cell Biol* **204**, 231-245 (2014).
996 107. J. Y. Tinevez *et al.*, TrackMate: An open and extensible platform for single-particle
997 tracking. *Methods* **115**, 80-90 (2017).
998 108. T. K. Lee *et al.*, A dynamically assembled cell wall synthesis machinery buffers cell
999 growth. *Proc Natl Acad Sci U S A* **111**, 4554-4559 (2014).
1000 109. G. Ozbaykal *et al.*, The transpeptidase PBP2 governs initial localization and
1001 activity of the major cell-wall synthesis machinery in E. coli. *Elife* **9** (2020).
1002 110. C. H. Bohrer, J. Xiao, Complex Diffusion in Bacteria. *Adv Exp Med Biol* **1267**, 15-
1003 43 (2020).
1004 111. A. Kusumi, Y. Sako, M. Yamamoto, Confined lateral diffusion of membrane
1005 receptors as studied by single particle tracking (nanovid microscopy). Effects of
1006 calcium-induced differentiation in cultured epithelial cells. *Biophys J* **65**, 2021-2040
1007 (1993).

1008 112. L. Pasquina-Lemonche *et al.*, The architecture of the Gram-positive bacterial cell
1009 wall. *Nature* **582**, 294-297 (2020).
1010 113. S. Middlemiss *et al.*, Molecular motor tug-of-war regulates elongasome cell wall
1011 synthesis dynamics in Bacillus subtilis. *bioRxiv*
1012 10.1101/2023.05.10.540107, 2023.2005.2010.540107 (2023).
1013 114. Z. Lyu *et al.*, FtsN maintains active septal cell wall synthesis by forming a
1014 processive complex with the septum-specific peptidoglycan synthases in E. coli.
1015 *Nat Commun* **13**, 5751 (2022).
1016 115. D. Straume *et al.*, Class A PBPs have a distinct and unique role in the construction
1017 of the pneumococcal cell wall. *Proc Natl Acad Sci U S A* **117**, 6129-6138 (2020).
1018 116. W. M. Figueroa-Cuilan, P. J. B. Brown, Cell Wall Biogenesis During Elongation
1019 and Division in the Plant Pathogen Agrobacterium tumefaciens. *Curr Top Microbiol*
1020 *Immunol* **418**, 87-110 (2018).
1021 117. M. A. Williams *et al.*, Unipolar Peptidoglycan Synthesis in the Rhizobiales Requires
1022 an Essential Class A Penicillin-Binding Protein. *mBio* **12**, e0234621 (2021).
1023 118. A. R. Winther, M. Kjos, M. L. Herigstad, L. S. Havarstein, D. Straume, EloR
1024 interacts with the lytic transglycosylase MltG at midcell in Streptococcus
1025 pneumoniae R6. *J Bacteriol* 10.1128/JB.00691-20 (2021).

1026

1027 **FIGURE LEGENDS**

1028 **Fig. 1.** Elongation PG synthesis proteins display processive circumferential motion,
1029 and a limited number of molecules engage in PG synthesis simultaneously. Sm-TIRFm
1030 was performed at 1 FPS as described in *Materials and Methods* on strains *iht-pbp2b*
1031 (IU15928), *iht-pbp2b* // P_{Zn}-*iht-pbp2b* (IU16553), *iht-rodA* (IU15970), *iht-rodA* // P_{Zn}-*iht-*
1032 *rodA* (IU16496), *iht-mreC* (IU16344), *iht-pbp1a* (IU16320), *iht-pbp1a* // P_{Zn}-*iht-pbp1a*
1033 (IU16497) and *iht-mpgA* (IU15997). (*A*) Representative time-lapse images and
1034 kymographs of molecules displaying processive circumferential movement in strains
1035 IU15928, IU15970, IU16344 and IU16497. Cell outlines are green (DICm) and HT-labeled
1036 molecules are magenta. Location of lines used to make kymographs are shown in the
1037 time lapse images (yellow dashed lines). For each protein, the left kymograph was
1038 generated from the cell depicted in the time-lapse images. Numbers (1-3) denote when
1039 each image in the time lapse was taken. The other two kymographs are from cells that

are not shown. Calculation of circumferential velocities from kymographs are described in *Materials and Methods*. Scale bars are 1 μm. (*B*) Movement patterns of HT-labeled molecules. Bars represent the mean relative frequency of each type of motion. For a given strain or condition, the relative frequencies of circumferential, diffusive, and static molecules were determined for each biological replicate. Frequencies were then averaged over all replicates to determine the mean (error bars represent ± SD). Mean values are annotated above each bar, and the total number of molecules analyzed (n) from the number of independent biological replicates (R) for each strain is below each strain or condition. Circumferential (red), diffusive (blue), and static (grey) movement patterns are shown. Circumferentially moving molecules were defined as molecules moving in one direction for 6 or more frames (at 1 FPS imaging rate) with a linear velocity ≥ 5 nm/s. Static molecules were defined as molecules not moving or moving for 6 or more frames with a velocity < 5 nm/s. Diffusive molecules were defined as molecules that moved, but not in a consistent direction, for 6 or more non-consecutive frames within a period of 90 s. Full criteria for determining movement patterns are described in *Materials and Methods*. The expression level of iHT-fusion proteins relative to the untagged WT level is shown as a percentage under the strain names. iHT-fusion proteins are expressed solely from the native chromosomal locus or with an additional copy of the gene encoding the iHT-fusion protein at an ectopic site under control of a zinc-inducible promoter, with 0 or 0.25 mM Zn inducer added. Unpaired t-tests were performed to compare relative frequencies of motion types. *ns* (nonsignificant), $^{*}P < 0.05$, $^{**}P < 0.01$, $^{***}P < 0.001$, $^{****}P < 0.0001$.

1062 **Fig. 2.** Diffusively moving components of the core PG elongasome do not actively
1063 synthesize PG (blue) in non-midcell regions of exponentially growing pneumococcal cells.
1064 3D-SIM images, where iHT-bPBP2b is red, regions of PBP transpeptidase activity is blue,
1065 and midcell regions include septa of dividing cells and equators of predivisional daughter
1066 cells. Cells were grown in BHI ± 0.3 mM Zn inducer, labeled with a saturating amount of
1067 HT-ligand for 15 min, washed, labeled with 400 μM of the fluorescent D-amino acid HADA
1068 (blue) for 2.5 min, fixed, and imaged as described in *Materials and Methods*. Images are
1069 summed from 15 *Z* plane sections (*Z*-stack) representing a total depth of 1.875 μm.
1070 Percentages indicate the amount of iHT-bPBP2b expressed relative to the untagged WT
1071 bPBP2b^{+} level (32). (*A*) *iht-pbp2b* (IU15928) and (*B*) *iht-pbp2b* // P_{Zn}-*iht-pbp2b* (IU16553).
1072 Scale bar is 1 μm.

1073 **Fig. 3.** bPBP2b, RodA, and MreC form a stable complex during active PG synthesis.
1074 Dot plots of (*A*) circumferential velocities and (*B*) circumferential durations of elongation
1075 PG synthesis proteins determined by sm-TIRFm at 1 FPS. Strains are the same as in Fig.
1076 1. +Zn condition indicates 0.25 mM Zn inducer was added. Black and red lines are means
1077 ± SD. n = total molecules analyzed from 2-5 independent biological replicates. Dotted
1078 grey lines indicate the minimum thresholds for (*A*) velocity (5 nm/s) and (*B*) duration (6
1079 s). A Kruskal-Wallis with Dunn's multiple comparisons test was used to compare
1080 circumferential velocities or circumferential durations in different strains. *ns*
1081 (nonsignificant), $^{**}P < 0.01$, $^{***}P < 0.001$, $^{****}P < 0.0001$.

1082 **Fig. 4.** Circumferential movement of bPBP2b and RodA is independent of FtsZ
1083 treadmilling and reflective of PG synthesis. Sm-TIRFm was performed at 1 FPS on strains
1084 expressing iHT-bPBP2b or iHT-RodA. Dot plots of circumferential velocities are shown

1085 with mean values ± SD indicated. (*A*) Both *iht-pbp2b* (black, IU15928) and *iht-pbp2b* P_{Zn}-
1086 *ftsZ*(D214A) (red, IU16091) strains were supplemented with 0.25 mM Zn inducer. (*B*)
1087 IU16056 expresses both iHT-bPBP2b and FtsZ-sfGFP. The treadmilling velocity of FtsZ-
1088 sfGFP filaments (green) and the circumferential velocity of iHT-bPBP2b single molecules
1089 (red) were determined. (*C*) *iht-pbp2b* (black, IU15928) and *iht-pbp2b* Δ*murZ* (red,
1090 IU16110) strains. (*D*) *iht-rodA* (black, IU15970) and *iht-rodA* Δ*murZ* (blue, IU16112)
1091 strains. n = total molecules analyzed from 2 biologically independent replicates.
1092 Circumferential velocities in different strains were compared using a Mann-Whitney test.
1093 * $P < 0.05$, **** $P < 0.0001$.

1094 **Fig. 5.** The catalytic activities of bPBP2b and RodA are required for cell viability and
1095 PG synthesis, but not localization. (*A*) Diagram of merodiploid strains containing catalytic
1096 mutant alleles fused to the HaloTag at the native locus and the Zn-inducible WT allele at
1097 the ectopic site. (*B*) Representative growth curves of WT (black square, IU1824), *iht-*
1098 *pbp2b* (red square, IU15928), *iht-rodA* (blue square, IU15970), Δ*pbp2b* // P_{Zn}-*pbp2b*
1099 (green, IU11258), *iht-pbp2b*(S391A) // P_{Zn}-*pbp2b* (red, IU16232), and *iht-rodA*(D283A) //
1100 P_{Zn}-*rodA* (blue, IU16239) strains grown in C+Y medium with or without 0.2 mM Zn inducer
1101 as described in the section on ectopic expression and depletion conditions in *Materials*
1102 *and Methods*. The experiment was repeated twice with similar results. (*C* and *D*) sm-
1103 TIRFm was performed at 1 FPS on strains IU16232 and IU16239. (*C*) Movement patterns
1104 of iHT-bPBP2b(S391A) (IU16232) and iHT-RodA(D283A) (IU16239). The layout is the
1105 same as Fig. 1*B* (see legend for details). Unpaired t-tests were performed to compare
1106 relative frequencies of motion types. *ns* (nonsignificant), ** $P < 0.01$, *** $P < 0.001$, **** $P <$
1107 0.0001. (*D*) Representative montages and kymographs of static molecules from strains

1108 IU16232 and IU16239 (without Zn inducer for 3 h) are displayed as described for Fig. 1*A*,
1109 except the scale bar is 0.5 µm. (*E*) 2D-FM of catalytically inactive proteins. Strains
1110 IU16232 and IU16239 were grown without Zn (see Fig. 5*B*) and labeled with saturating
1111 amounts of HT-ligand. HT-fusion proteins are shown in magenta. Scale bar is 1 µm. The
1112 experiment was repeated twice with similar results.

1113 **Fig. 6.** bPBP2b localization becomes diffuse and circumferential movement is lost
1114 upon MreC depletion. (*A*) 2D-FM of strains *iht-pbp2b* (left, IU15928) and *iht-pbp2b* Δ*mreC*
1115 // P_{Zn}-*mreC* (right, IU16281). Cells were grown in C+Y media with or without (depletion)
1116 0.2 mM Zn inducer, labeled with saturating amounts of HT-ligand, and imaged after 3 h.
1117 See the section on ectopic expression and depletion conditions in *Materials and Methods*
1118 for details. The experiment was repeated twice with similar results. (*B*) sm-TIRFm was
1119 performed at 1 FPS on strains *iht-pbp2b* (IU15928) and *iht-pbp2b* Δ*mreC* // P_{Zn}-*mreC*
1120 (IU16281) after 3 h of growth in C+Y media without Zn inducer (depletion). The layout is
1121 the same as Fig. 1*B* (see legend for details). Unpaired t-tests were performed to compare
1122 relative frequencies of motion types. *ns* (nonsignificant), $^{*}P < 0.05$, $^{**}P < 0.01$.

1123 **Fig. 7.** bPBP2b and RodA require each other for localization and motion. 2D-FM and
1124 sm-TIRFm at 1 FPS were performed on strains *iht-pbp2b* Δ*rodA* // P_{Zn}-*rodA* (IU16204)
1125 and *iht-rodA* Δ*pbp2b* // P_{Zn}-*pbp2b* (IU16202). (*A* and *B*) 2D-FM showing localization in
1126 cells of strains (*A*) iHT-bPBP2b (IU16204) and (*B*) iHT-RodA (IU16202) grown with or
1127 without (depletion; depl.) 0.2 mM Zn inducer for 3 h and labeled with saturating amounts
1128 of HT-ligand. See the section on ectopic expression and depletion conditions in *Materials*
1129 *and Methods* for additional details. The experiment was repeated twice with similar
1130 results. (*C* to *E*) sm-TIRFm was performed at 1 FPS on IU16204 and IU16202 without Zn

1131 inducer (depletion) for 3 hours. (*C*) Movement patterns of HT-labeled molecules. Results
1132 for the *iht-pbp2b* Δ*rodA* // P_{Zn}-*rodA* (IU16204) and *iht-rodA* Δ*pbp2b* // P_{Zn}-*pbp2b* (IU16202)
1133 strains were determined and are graphed with data for *iht-pbp2b* (IU15928) and *iht-rodA*
1134 (IU15970) replotted from Fig. 1*B* for comparison. The layout is the same as Fig. 1*B* (see
1135 legend for details). Unpaired t-tests were performed to compare relative frequencies of
1136 motion types. *ns* (nonsignificant), *$P < 0.05$, **$P < 0.01$, ***$P < 0.001$. (*D* and *E*) Dot plots
1137 of circumferential velocities with mean values ± SD indicated for (*D*) strains IU15928
1138 (black) and IU16204 (red), and (*E*) strains IU15970 (black) and IU16202 (red). Data from
1139 stains IU15928 and IU15970 are replotted from Fig. 3*A* for comparison. n = total
1140 molecules analyzed from 2 biologically independent replicates. A Mann-Whitney test was
1141 used to compare velocities upon protein depletion (depl.). *ns* (nonsignificant).

1142 **Fig. 8.** Circumferential movement of aPBP1a reflects active PG synthesis. Sm-TIRFm
1143 was performed at 1 FPS as described in *Materials and Methods* on strains *iht-pbp1a* //
1144 P_{Zn}-*iht-pbp1a* (IU16497) and *iht-pbp1a*(S370A) // P_{Zn}-*iht-pbp1a*(S370A) (IU19168) with
1145 0.25 mM Zn added. Movement patterns of HT-labeled molecules at sites of PG synthesis
1146 (midcell) or elsewhere in the cell (non-midcell) were analyzed. The layout is the same as
1147 Fig. 1*B* (see legend for details). A two-way ANOVA with Tukey's multiple comparison test
1148 was used to compare relative frequencies of motion types among strains. * $P < 0.05$.

1149 **Fig. 9.** MpgA displays confined subdiffusive movement at midcell. Sm-TIRFm was
1150 performed on strains *iht-mpgA* (IU15997) and *iht-mreC* (IU16344). Representative
1151 kymographs of (*A*) iHT-MpgA molecules moving at sites of PG synthesis imaged at 1 FPS
1152 and (*B*) iHT-MpgA and iHT-MreC molecules imaged at 10 FPS. (*C*) Dot plots of velocities
1153 determined at 10 FPS over short runs of iHT-MpgA molecules in midcell regions (black)

1154 and at non-midcell regions (red). Mean values ± SD are indicated. n = total molecules
1155 analyzed from 2 biologically independent replicates. Velocities in different regions of cells
1156 were compared using a Mann-Whitney test. ****, $P < 0.0001$.

1157 **Fig. 10.** Components of the pneumococcal core PG elongasome and proteins
1158 implicated in elongation PG synthesis exhibit different patterns of confined diffusion. Sm-
1159 TIRFm was performed at 20 FPS on strains *iht-pbp2b* // P_{Zn}-*iht-pbp2b* (IU16553), *iht-rodA*
1160 // P_{Zn}-*iht-rodA* (IU16496), *iht-mreC* (IU16344), *iht-pbp1a* // P_{Zn}-*iht-pbp1a* (IU16497) and
1161 *iht-mpgA* (IU15997). 0.25 mM Zn inducer was added to strains IU16553, IU16496 and
1162 IU16497. (*A*) Representative fields of cells containing multiple single-molecule
1163 trajectories (colored lines) classified as diffusive (top row) and non-diffusive (bottom row).
1164 Trajectories with a displacement > 0.13 μm and a velocity standard deviation > 0.63 μm/s
1165 were defined as diffusive, and the remaining trajectories were defined as non-diffusive.
1166 Full details of trajectory constructions and classification criteria are described in *Materials*
1167 *and Methods*. The color of each trajectory line segment represents the displacement (in
1168 nm) of the molecule from one frame to the next. Scale bar is 1 μm. (*B*) Mean square
1169 displacements (MSD) were calculated for diffusive and non-diffusive trajectories. Circles
1170 show MSD values, and error bars represent SEM. Lines represent MSD curves fit to the
1171 data as described in *Materials and Methods*. To the right of the graph are the mean
1172 diffusion coefficients (± SEM) of diffusive trajectories, alpha values of diffusive trajectories
1173 (α), the percent of total trajectories that were classified as diffusive (% diffusive), and the
1174 total number of trajectories (n) analyzed from 2 biologically independent replicates. α
1175 values < 1 indicate that molecules are exhibiting confined diffusion (or subdiffusion),
1176 discussed in the text. The diffusion coefficients were compared between strains using a

1177 Brown-Forsythe and Welch's ANOVA with a Games-Howell multiple comparisons test. **
1178 $P < 0.01$.

1179 **Fig. 11.** Summary model of (*A*) the composition and dynamics of core elongasome
1180 components (bPBP2b, RodA, and MreC) and proteins linked to PG elongation synthesis
1181 (aPBP1a and MpgA) in growing *S. pneumoniae* cells; and (*B*) the distribution of these
1182 proteins when underexpressed (left) or expressed at WT levels (right). (*A*) The
1183 circumferential, processive movement of bPBP2b, RodA, and MreC reported here likely
1184 apply to the other core elongasome components RodZ and MreD. In early, predivisional
1185 cells, the core PG elongasome is located in the FtsZ-ring at the equator midcell of a
1186 daughter cell. In later divisional cells, the core PG elongasome is in the outer ring of the
1187 midcell septal annular disk. The motion of MreC is the same in early or late divisional
1188 cells. Class A aPBP1a also displays circumferential, processive motion at midcell that
1189 depends on PG synthesis, but its dynamics indicate that aPBP1a is not a persistent
1190 member of the core PG elongasome, although short interactions are possible. In contrast,
1191 MpgA moves in a distinctive type of subdiffusion that is largely confined to the midcell
1192 region. Components of the core elongasome and aPBP1a move diffusively outside of
1193 midcell rings. There are also nonmoving, static molecules (> 6 s) of elongasome proteins
1194 and aPBP1a, mainly in midcell regions. It is not clear whether static molecules are
1195 synthesizing PG or are in a non-synthesizing transition state. In addition, diffusing
1196 molecules of aPBP1a and MpgA were infrequently detected pausing (< 1s) before
1197 resuming motion. See text for additional information. (*B*) When underexpressed,
1198 components of the core PG elongasome are largely confined to PG synthesis at midcell
1199 septa and the equators of predivisional daughter cells starting to divide. In contrast, when

1200 expressed at WT levels, most components of the PG elongasome (and aPBP1a) are
1201 diffusing over the cell surface and are not synthesizing PG. Thus, elongasome
1202 components and aPBP1a are in excess in growing cells, and only a limited number
1203 engage in midcell PG synthesis. In contrast, subdiffusion of MpgA molecules expressed
1204 at the WT level is largely confined to the midcell region by an unknown mechanism. See
1205 text for additional details.

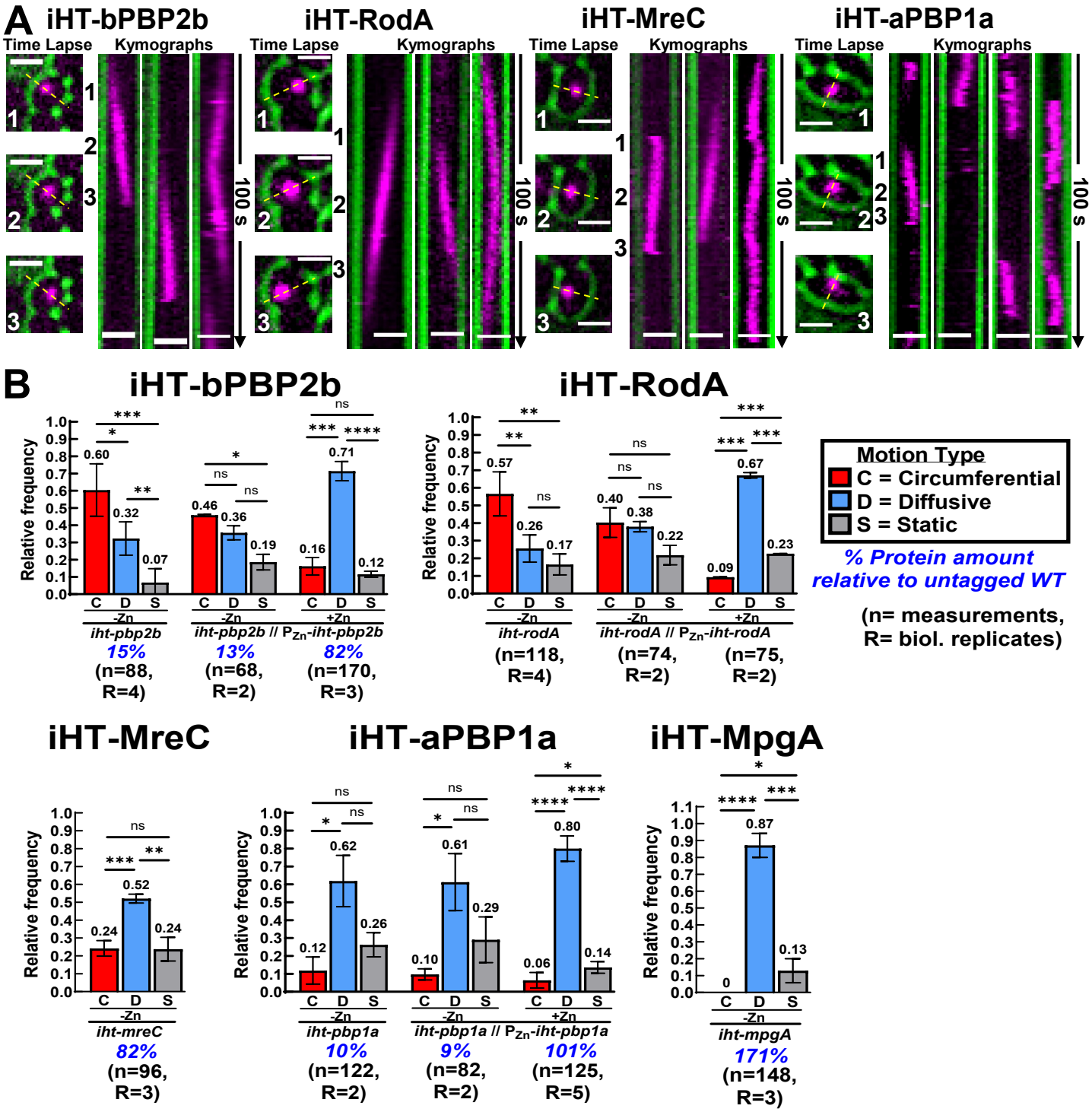
A
iHT-bPBP2b
iHT-RodA
iHT-MreC
iHT-aPBP1a
Time Lapse
Kymographs
100 s
B
iHT-bPBP2b
Relative frequency
0.60
0.32
0.07
0.46
0.36
0.19
0.16
0.71
0.12
C D S
-Zn
+Zn
iht-pbp2b
iht-pbp2b // PZn-iht-pbp2b
15%
(n=88, R=4)
13%
(n=68, R=2)
82%
(n=170, R=3)
iHT-RodA
0.57
0.26
0.17
0.40
0.38
0.22
0.09
0.67
0.23
iht-rodA
iht-rodA // PZn-iht-rodA
(n=118, R=4)
(n=74, R=2)
(n=75, R=2)
Motion Type
C = Circumferential
D = Diffusive
S = Static
% Protein amount relative to untagged WT
(n= measurements, R= biol. replicates)
iHT-MreC
0.24
0.52
0.24
iht-mreC
82%
(n=96, R=3)
iHT-aPBP1a
0.12
0.62
0.26
0.10
0.61
0.29
0.06
0.80
0.14
iht-pbp1a
iht-pbp1a // PZn-iht-pbp1a
10%
(n=122, R=2)
9%
(n=82, R=2)
101%
(n=125, R=5)
iHT-MpgA
0
0.87
0.13
iht-mpgA
171%
(n=148, R=3)

Fig. 1.

Fig. 1. Elongation PG synthesis proteins display processive circumferential motion, and a limited number of molecules engage in PG synthesis simultaneously. Sm-TIRFm was performed at 1 FPS as described in *Materials and Methods* on strains *iht-pbp2b* (IU15928), *iht-pbp2b* // P_{Zn}-*iht-pbp2b* (IU16553), *iht-rodA* (IU15970), *iht-rodA* // P_{Zn}-*iht-rodA* (IU16496), *iht-mreC* (IU16344), *iht-pbp1a* (IU16320), *iht-pbp1a* // P_{Zn}-*iht-pbp1a* (IU16497) and *iht-mpgA* (IU15997). (*A*) Representative time-lapse images and kymographs of molecules displaying processive circumferential movement in strains IU15928, IU15970, IU16344 and IU16497. Cell outlines are green (DICm) and HT-labeled molecules are magenta. Location of lines used to make kymographs are shown in the time lapse images (yellow dashed lines). For each protein, the left kymograph was generated from the cell depicted in the time-lapse images. Numbers (1-3) denote when each image in the time lapse was taken. The other two kymographs are from cells that are not shown. Calculation of circumferential velocities from kymographs are described in *Materials and Methods*. Scale bars are 1 μm. (*B*) Movement patterns of HT-labeled molecules. Bars represent the mean relative frequency of each type of motion. For a given strain or condition, the relative frequencies of circumferential, diffusive, and static molecules were determined for each biological replicate. Frequencies were then averaged over all replicates to determine the mean (error bars represent ± SD). Mean values are annotated above each bar, and the total number of molecules analyzed (n) from the number of independent biological replicates (R) for each strain are below each strain or condition. Circumferential (red), diffusive (blue), and static (grey) movement patterns are shown. Circumferentially moving molecules were defined as molecules moving in one direction for 6 or more frames (at 1 FPS imaging rate) with a linear velocity ≥ 5 nm/s. Static molecules were defined as molecules not moving or moving for 6 or more frames with a velocity < 5 nm/s. Diffusive molecules were defined as molecules that moved, but not in a consistent direction, for 6 or more non-consecutive frames within a period of 90 s. Full criteria for determining movement patterns are described in *Materials and Methods*. The expression level of iHT-fusion proteins relative to the untagged WT level is shown as a percentage under the strain names. iHT-fusion proteins are expressed solely from the native chromosomal locus or with an additional copy of the gene encoding the iHT-fusion protein at an ectopic site under control of a zinc-inducible promoter, with 0 or 0.25 mM Zn inducer added. Unpaired t-tests were performed to compare relative frequencies of motion types. *ns* (nonsignificant), $^{*}P < 0.05$, $^{**}P < 0.01$, $^{***}P < 0.001$, $^{****}P < 0.0001$.

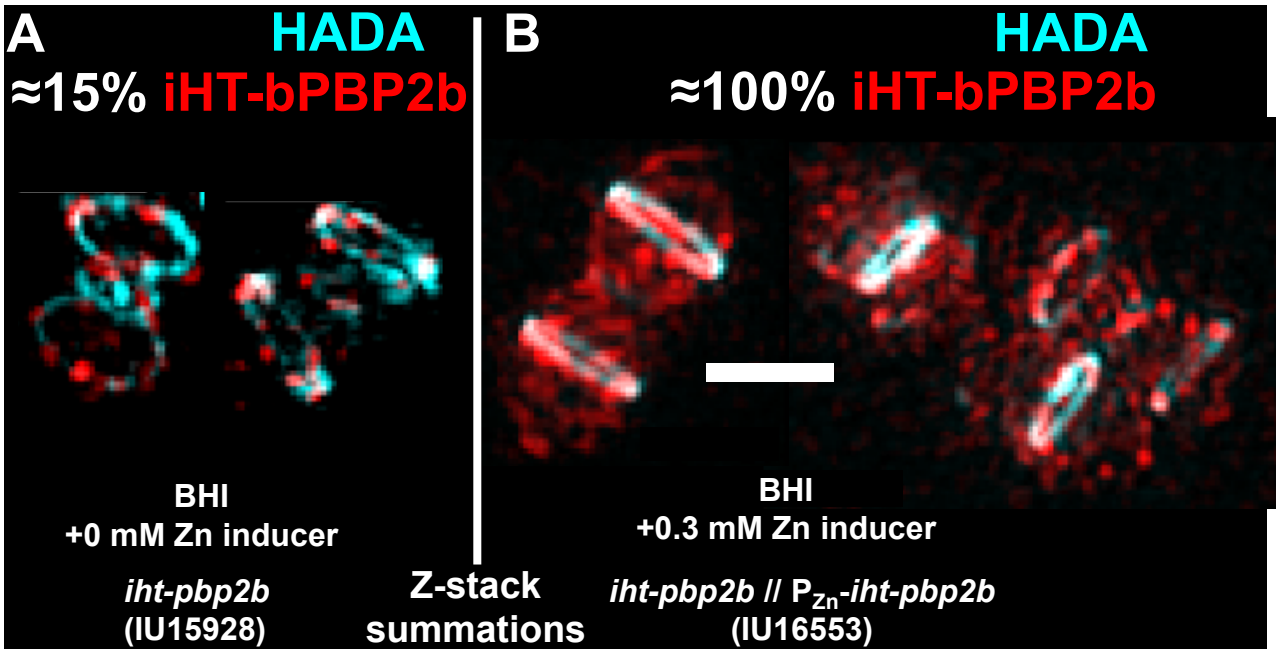

Fig. 2. Diffusively moving components of the core PG elongasome do not actively synthesize PG (blue) in non-midcell regions of exponentially growing pneumococcal cells. 3D-SIM images, where iHT-bPBP2b is red, regions of PBP transpeptidase activity is blue, and midcell regions include septa of dividing cells and equators of predivisional daughter cells. Cells were grown in BHI ± 0.3 mM Zn inducer, labeled with a saturating amount of HT-ligand for 15 min, washed, labeled with 400 μM of the fluorescent D-amino acid HADA (blue) for 2.5 min, fixed, and imaged as described in *Materials and Methods*. Images are summed from 15 *Z* plane sections (*Z*-stack) representing a total depth of 1.875 μm. Percentages indicate the amount of iHT-bPBP2b expressed relative to the untagged WT bPBP2b^{+} level (32). (*A*) *iht-pbp2b* (IU15928) and (*B*) *iht-pbp2b* // P_{Zn}-*iht-pbp2b* (IU16553). Scale bar is 1 μm.

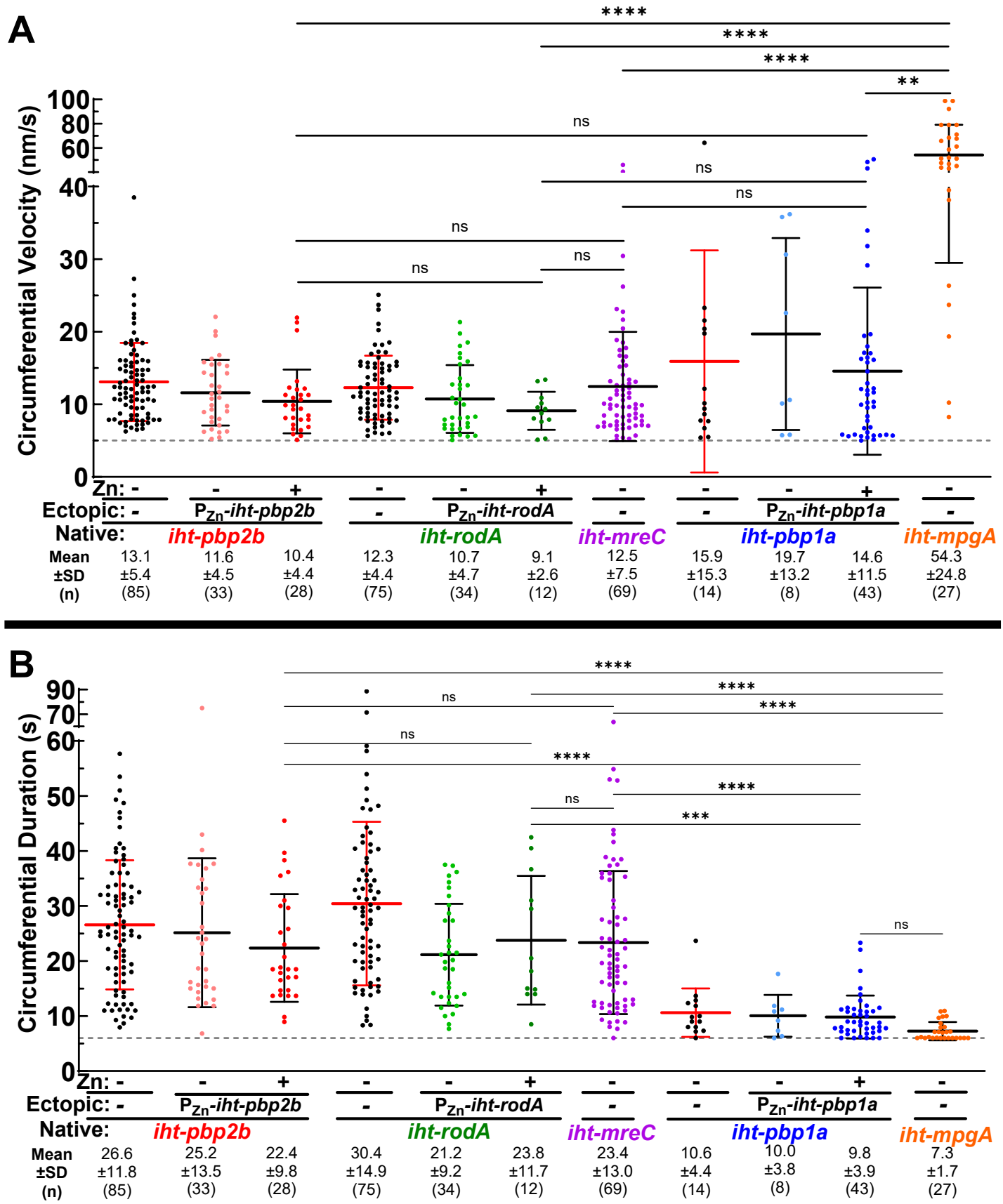
A
Circumferential Velocity (nm/s)
100
80
60
40
30
20
10
0
****
****
****
**
ns
ns
ns
ns
ns
ns
Zn: - - + - - + - - - + -
Ectopic: - PZn-iht-pbp2b - PZn-iht-rodA - - PZn-iht-pbp1a -
Native: iht-pbp2b iht-rodA iht-mreC iht-pbp1a iht-mpgA
Mean ±SD (n)
13.1 ±5.4 (85)
11.6 ±4.5 (33)
10.4 ±4.4 (28)
12.3 ±4.4 (75)
10.7 ±4.7 (34)
9.1 ±2.6 (12)
12.5 ±7.5 (69)
15.9 ±15.3 (14)
19.7 ±13.2 (8)
14.6 ±11.5 (43)
54.3 ±24.8 (27)
B
Circumferential Duration (s)
90
70
60
50
40
30
20
10
0
****
****
****
ns
ns
****
****
ns
***
ns
Zn: - - + - - + - - - + -
Ectopic: - PZn-iht-pbp2b - PZn-iht-rodA - - PZn-iht-pbp1a -
Native: iht-pbp2b iht-rodA iht-mreC iht-pbp1a iht-mpgA
Mean ±SD (n)
26.6 ±11.8 (85)
25.2 ±13.5 (33)
22.4 ±9.8 (28)
30.4 ±14.9 (75)
21.2 ±9.2 (34)
23.8 ±11.7 (12)
23.4 ±13.0 (69)
10.6 ±4.4 (14)
10.0 ±3.8 (8)
9.8 ±3.9 (43)
7.3 ±1.7 (27)

Fig. 3.

Fig. 3. bPBP2b, RodA, and MreC form a stable complex during active PG synthesis. Dot plots of (*A*) circumferential velocities and (*B*) circumferential durations of elongation PG synthesis proteins determined by sm-TIRFm at 1 FPS. Strains are the same as in Fig. 1. +Zn condition indicates 0.25 mM Zn inducer was added. Black and red lines are means ± SD. n = total molecules analyzed from 2-5 independent biological replicates. Dotted grey lines indicate the minimum thresholds for (*A*) velocity (5 nm/s) and (*B*) duration (6 s). A Kruskal-Wallis with Dunn's multiple comparisons test was used to compare circumferential velocities or circumferential durations in different strains. *ns* (nonsignificant), $^{**}P < 0.01$, $^{***}P < 0.001$, $^{****}P < 0.0001$.

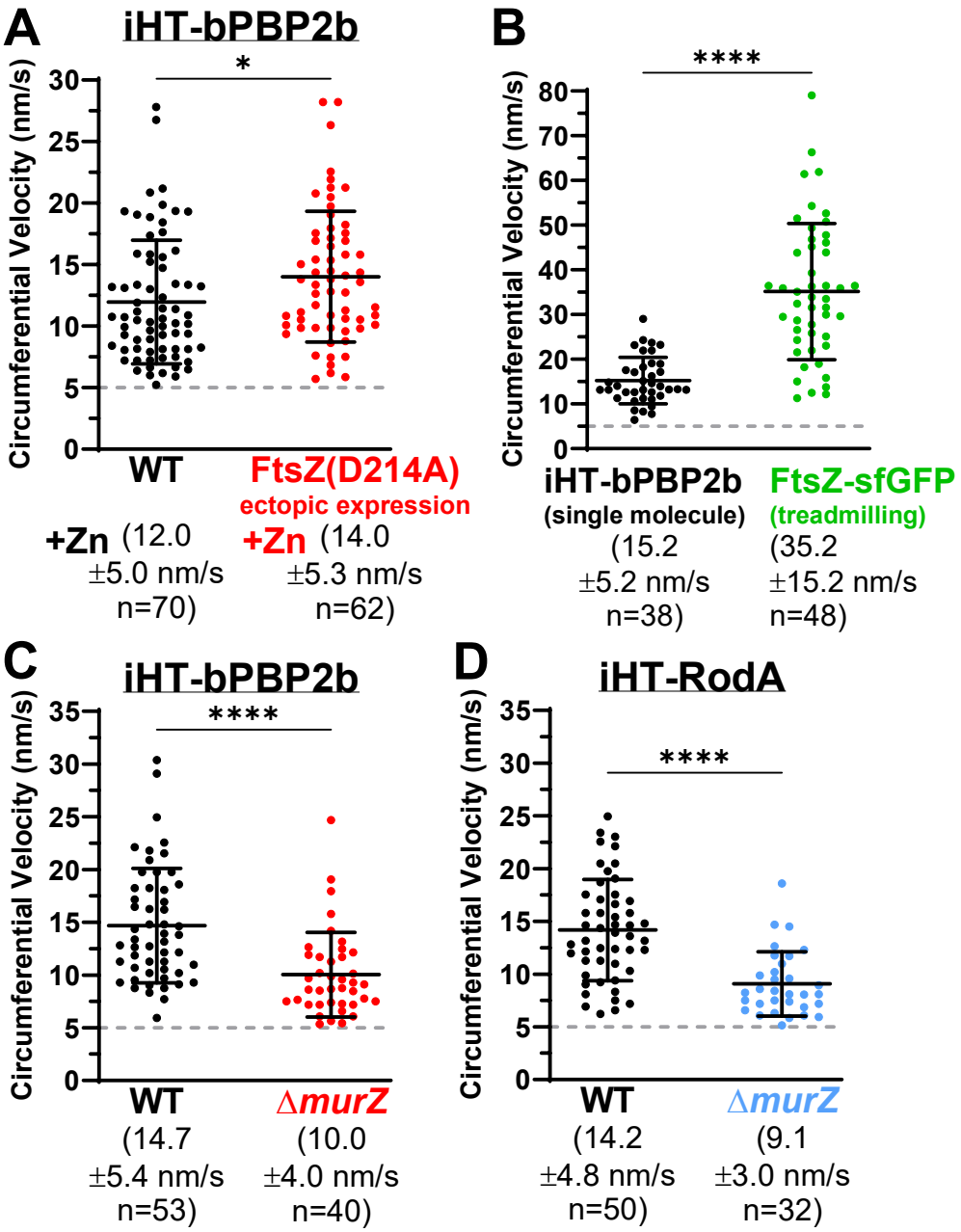

Fig. 4. Circumferential movement of bPBP2b and RodA is independent of FtsZ treadmilling and reflective of PG synthesis. Sm-TIRFm was performed at 1 FPS on strains expressing iHT-bPBP2b or iHT-RodA. Dot plots of circumferential velocities are shown with mean values ± SD indicated. (*A*) Both *iht-pbp2b* (black, IU15928) and *iht-pbp2b* P_{Zn}-*ftsZ*(D214A) (red, IU16091) strains were supplemented with 0.25 mM Zn inducer. (*B*) IU16056 expresses both iHT-bPBP2b and FtsZ-sfGFP. The treadmilling velocity of FtsZ-sfGFP filaments (green) and the circumferential velocity of iHT-bPBP2b single molecules (red) were determined. (*C*) *iht-pbp2b* (black, IU15928) and *iht-pbp2b* Δ*murZ* (red, IU16110) strains. (*D*) *iht-rodA* (black, IU15970) and *iht-rodA* Δ*murZ* (blue, IU16112) strains. n = total molecules analyzed from 2 biologically independent replicates. Circumferential velocities in different strains were compared using a Mann-Whitney test. * $P < 0.05$, **** $P < 0.0001$.

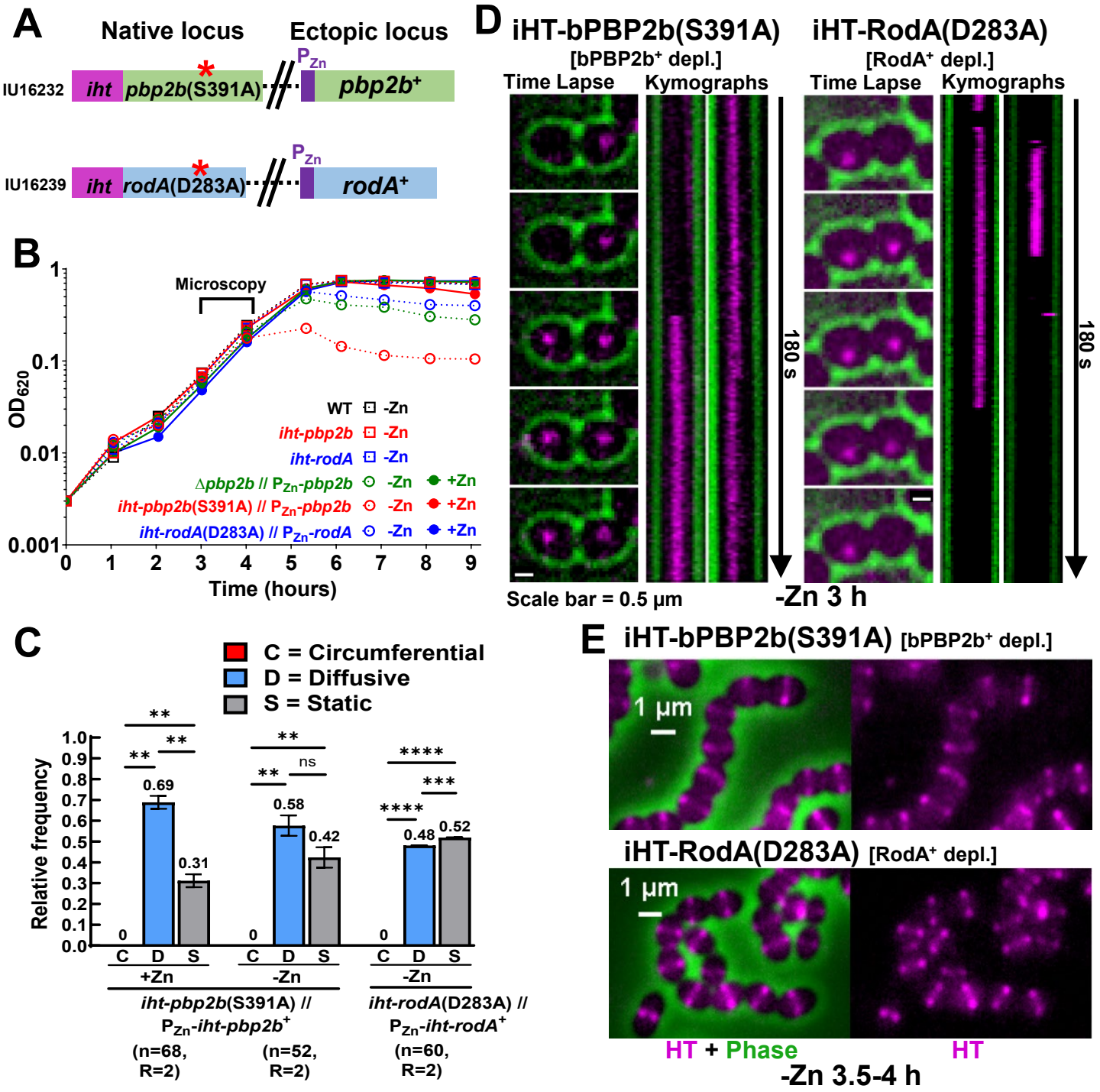
A
Native locus
Ectopic locus
IU16232
iht
pbp2b(S391A)
PZn
pbp2b+
IU16239
iht
rodA(D283A)
PZn
rodA+
B
Microscopy
OD620
Time (hours)
WT -Zn
iht-pbp2b -Zn
iht-rodA -Zn
Δpbp2b // PZn-pbp2b -Zn +Zn
iht-pbp2b(S391A) // PZn-pbp2b -Zn +Zn
iht-rodA(D283A) // PZn-rodA -Zn +Zn
C
C = Circumferential
D = Diffusive
S = Static
Relative frequency
0.69
0.31
0.58
0.42
0.48
0.52
+Zn
-Zn
-Zn
iht-pbp2b(S391A) // PZn-iht-pbp2b+
iht-rodA(D283A) // PZn-iht-rodA+
(n=68, R=2)
(n=52, R=2)
(n=60, R=2)
D
iHT-bPBP2b(S391A)
[bPBP2b+ depl.]
iHT-RodA(D283A)
[RodA+ depl.]
Time Lapse
Kymographs
Time Lapse
Kymographs
180 s
180 s
Scale bar = 0.5 µm
-Zn 3 h
E
iHT-bPBP2b(S391A) [bPBP2b+ depl.]
1 µm
iHT-RodA(D283A) [RodA+ depl.]
1 µm
HT + Phase
HT
-Zn 3.5-4 h

Fig. 5.

Fig. 5. The catalytic activities of bPBP2b and RodA are required for cell viability and PG synthesis, but not localization. (*A*) Diagram of merodiploid strains containing catalytic mutant alleles fused to the HaloTag at the native locus and the Zn-inducible WT allele at the ectopic site. (*B*) Representative growth curves of WT (black square, IU1824), *iht-pbp2b* (red square, IU15928), *iht-rodA* (blue square, IU15970), Δ*pbp2b* // P_{Zn}-*pbp2b* (green, IU11258), *iht-pbp2b*(S391A) // P_{Zn}-*pbp2b* (red, IU16232), and *iht-rodA*(D283A) // P_{Zn}-*rodA* (blue, IU16239) strains grown in C+Y medium with or without 0.2 mM Zn inducer as described in the section on ectopic expression and depletion conditions in *Materials and Methods*. The experiment was repeated twice with similar results. (*C* and *D*) sm-TIRFm was performed at 1 FPS on strains IU16232 and IU16239. (*C*) Movement patterns of iHT-bPBP2b(S391A) (IU16232) and iHT-RodA(D283A) (IU16239). The layout is the same as Fig. 1*B* (see legend for details). Unpaired t-tests were performed to compare relative frequencies of motion types. *ns* (nonsignificant), $^{**}P < 0.01$, $^{***}P < 0.001$, $^{****}P < 0.0001$. (*D*) Representative montages and kymographs of static molecules from strains IU16232 and IU16239 (without Zn inducer for 3 h) are displayed as described for Fig. 1*A*, except the scale bar is 0.5 μm. (*E*) 2D-FM of catalytically inactive proteins. Strains IU16232 and IU16239 were grown without Zn (see Fig. 5*B*) and labeled with saturating amounts of HT-ligand. HT-fusion proteins are shown in magenta. Scale bar is 1 μm. The experiment was repeated twice with similar results.

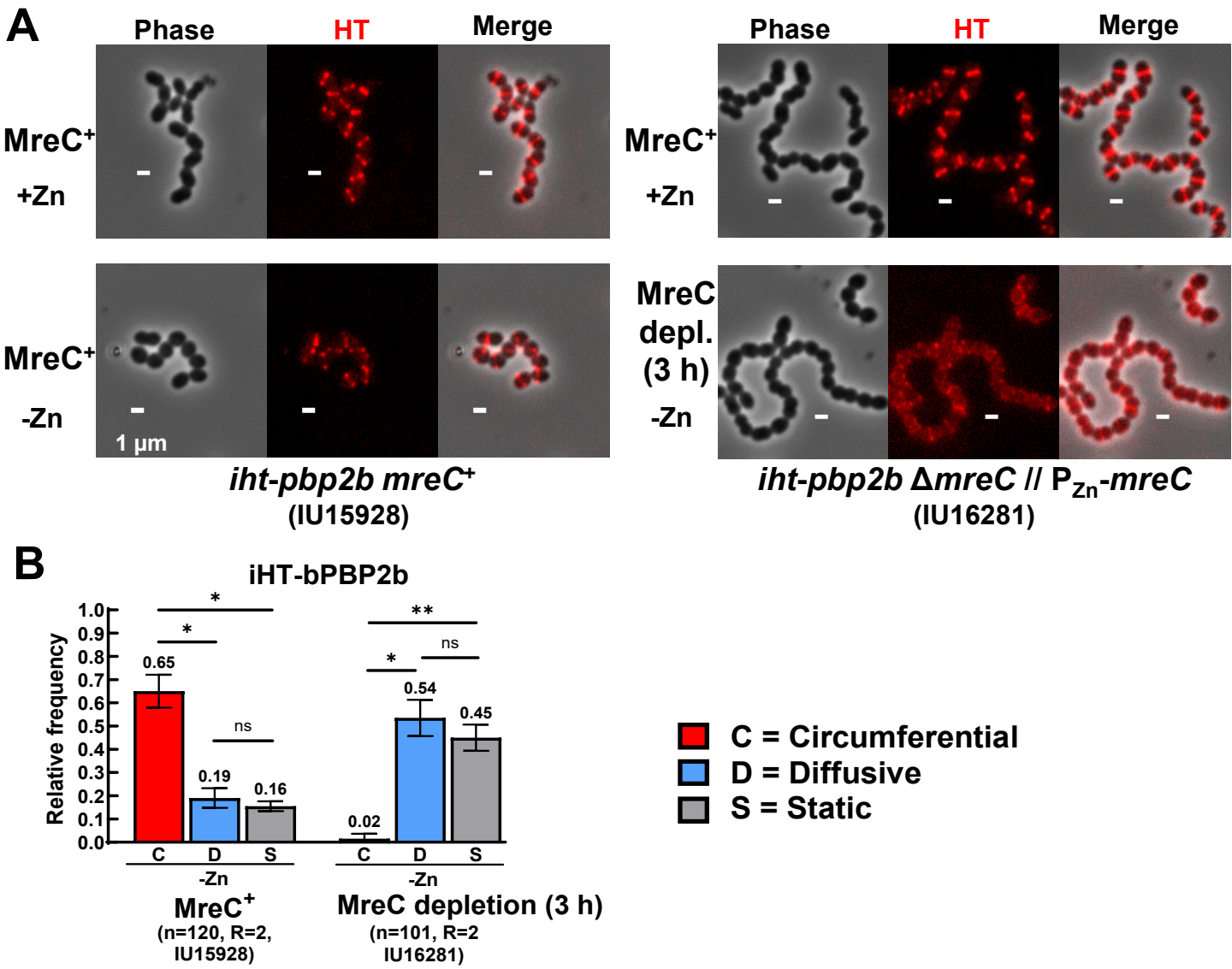

Fig. 6. bPBP2b localization becomes diffuse and circumferential movement is lost upon MreC depletion. (*A*) 2D-FM of strains *iht-pbp2b* (left, IU15928) and *iht-pbp2b* Δ*mreC* // P_{Zn}-*mreC* (right, IU16281). Cells were grown in C+Y media with or without (depletion) 0.2 mM Zn inducer, labeled with saturating amounts of HT-ligand, and imaged after 3 h. See the section on ectopic expression and depletion conditions in *Materials and Methods* for details. The experiment was repeated twice with similar results. (*B*) sm-TIRFm was performed at 1 FPS on strains *iht-pbp2b* (IU15928) and *iht-pbp2b* Δ*mreC* // P_{Zn}-*mreC* (IU16281) after 3 h of growth in C+Y media without Zn inducer (depletion). The layout is the same as Fig. 1*B* (see legend for details). Unpaired t-tests were performed to compare relative frequencies of motion types. *ns* (nonsignificant), $^{*}P < 0.05$, $^{**}P < 0.01$.

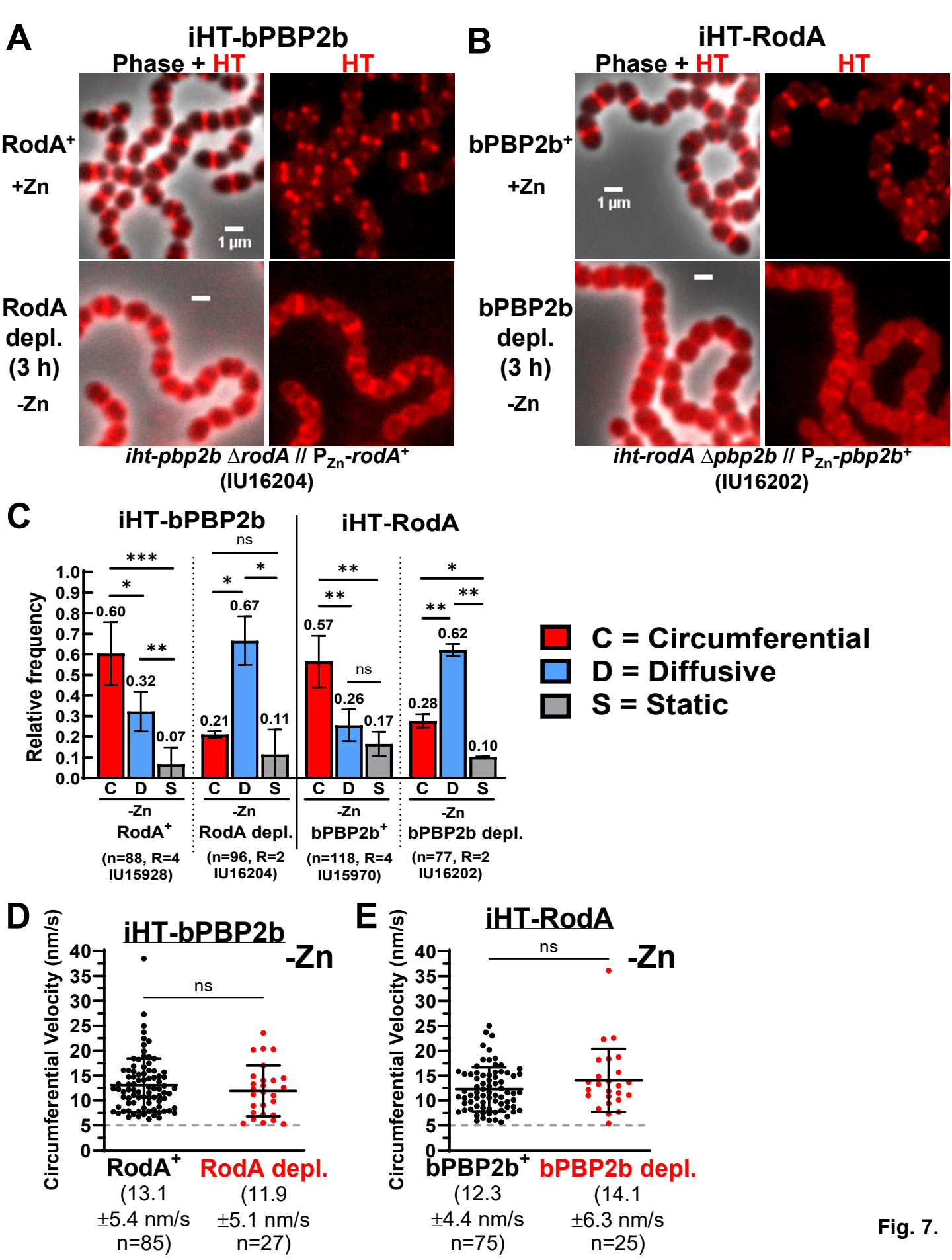
A
iHT-bPBP2b
Phase + HT
HT
RodA+
+Zn
1 µm
RodA
depl.
(3 h)
-Zn
iht-pbp2b ΔrodA // PZn-rodA+
(IU16204)
B
iHT-RodA
Phase + HT
HT
bPBP2b+
+Zn
1 µm
bPBP2b
depl.
(3 h)
-Zn
iht-rodA Δpbp2b // PZn-pbp2b+
(IU16202)
C
iHT-bPBP2b
iHT-RodA
Relative frequency
C = Circumferential
D = Diffusive
S = Static
-Zn
RodA+
(n=88, R=4
IU15928)
RodA depl.
(n=96, R=2
IU16204)
bPBP2b+
(n=118, R=4
IU15970)
bPBP2b depl.
(n=77, R=2
IU16202)
D
iHT-bPBP2b
-Zn
Circumferential Velocity (nm/s)
ns
RodA+
(13.1
±5.4 nm/s
n=85)
RodA depl.
(11.9
±5.1 nm/s
n=27)
E
iHT-RodA
-Zn
Circumferential Velocity (nm/s)
ns
bPBP2b+
(12.3
±4.4 nm/s
n=75)
bPBP2b depl.
(14.1
±6.3 nm/s
n=25)

Fig. 7.

Fig. 7. bPBP2b and RodA require each other for localization and motion. 2D-FM and sm-TIRFm at 1 FPS were performed on strains *iht-pbp2b* Δ*rodA* // P_{Zn}-*rodA* (IU16204) and *iht-rodA* Δ*pbp2b* // P_{Zn}-*pbp2b* (IU16202). (*A* and *B*) 2D-FM showing localization in cells of strains (*A*) iHT-bPBP2b (IU16204) and (*B*) iHT-RodA (IU16202) grown with or without (depletion; depl.) 0.2 mM Zn inducer for 3 h and labeled with saturating amounts of HT-ligand. See the section on ectopic expression and depletion conditions in *Materials and Methods* for additional details. The experiment was repeated twice with similar results. (*C* to *E*) sm-TIRFm was performed at 1 FPS on IU16204 and IU16202 without Zn inducer (depletion) for 3 hours. (*C*) Movement patterns of HT-labeled molecules. Results for the *iht-pbp2b* Δ*rodA* // P_{Zn}-*rodA* (IU16204) and *iht-rodA* Δ*pbp2b* // P_{Zn}-*pbp2b* (IU16202) strains were determined and are graphed with data for *iht-pbp2b* (IU15928) and *iht-rodA* (IU15970) replotted from Fig. 1*B* for comparison. The layout is the same as Fig. 1*B* (see legend for details). Unpaired t-tests were performed to compare relative frequencies of motion types. *ns* (nonsignificant), $^{*}P < 0.05$, $^{**}P < 0.01$, $^{***}P < 0.001$. (*D* and *E*) Dot plots of circumferential velocities with mean values ± SD indicated for (*D*) strains IU15928 (black) and IU16204 (red), and (*E*) strains IU15970 (black) and IU16202 (red). Data from stains IU15928 and IU15970 are replotted from Fig. 3*A* for comparison. n = total molecules analyzed from 2 biologically independent replicates. A Mann-Whitney test was used to compare velocities upon protein depletion (depl.). *ns* (nonsignificant).

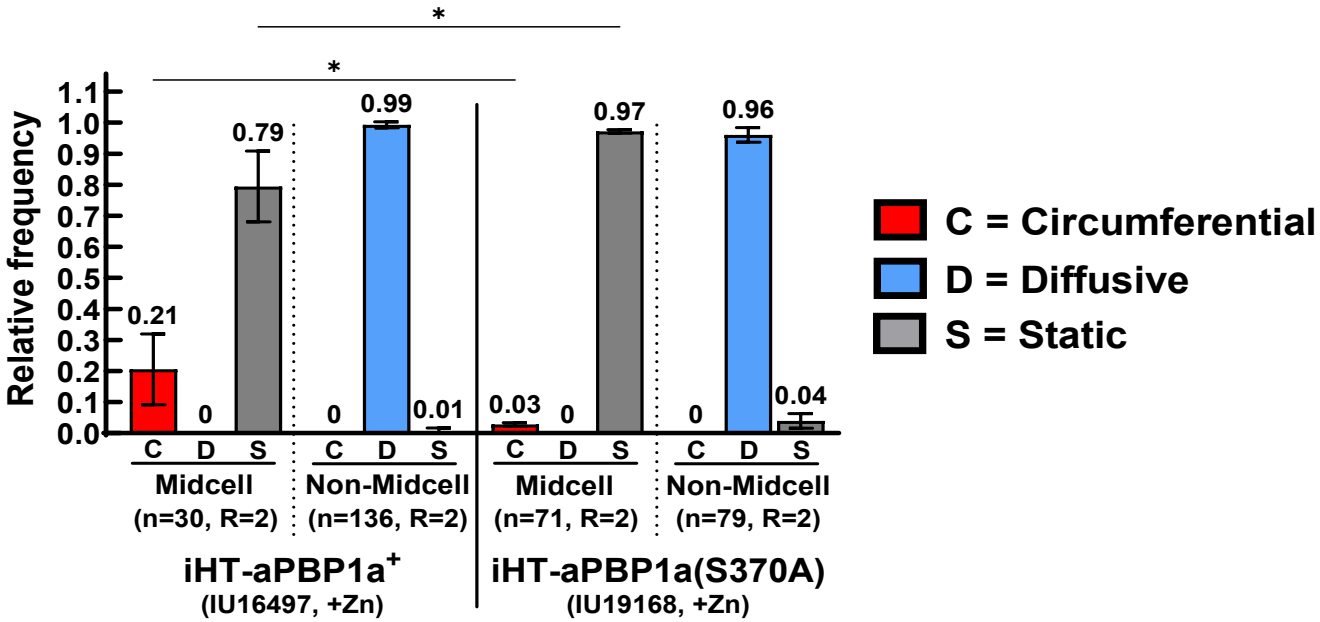

Fig. 8. Circumferential movement of aPBP1a reflects active PG synthesis. Sm-TIRFm was performed at 1 FPS as described in *Materials and Methods* on strains *iht-pbp1a* // P_{Zn}-*iht-pbp1a* (IU16497) and *iht-pbp1a*(S370A) // P_{Zn}-*iht-pbp1a*(S370A) (IU19168) with 0.25 mM Zn added. Movement patterns of HT-labeled molecules at sites of PG synthesis (midcell) or elsewhere in the cell (non-midcell) were analyzed. The layout is the same as Fig. 1*B* (see legend for details). A two-way ANOVA with Tukey's multiple comparison test was used to compare relative frequencies of motion types among strains. * $P < 0.05$.

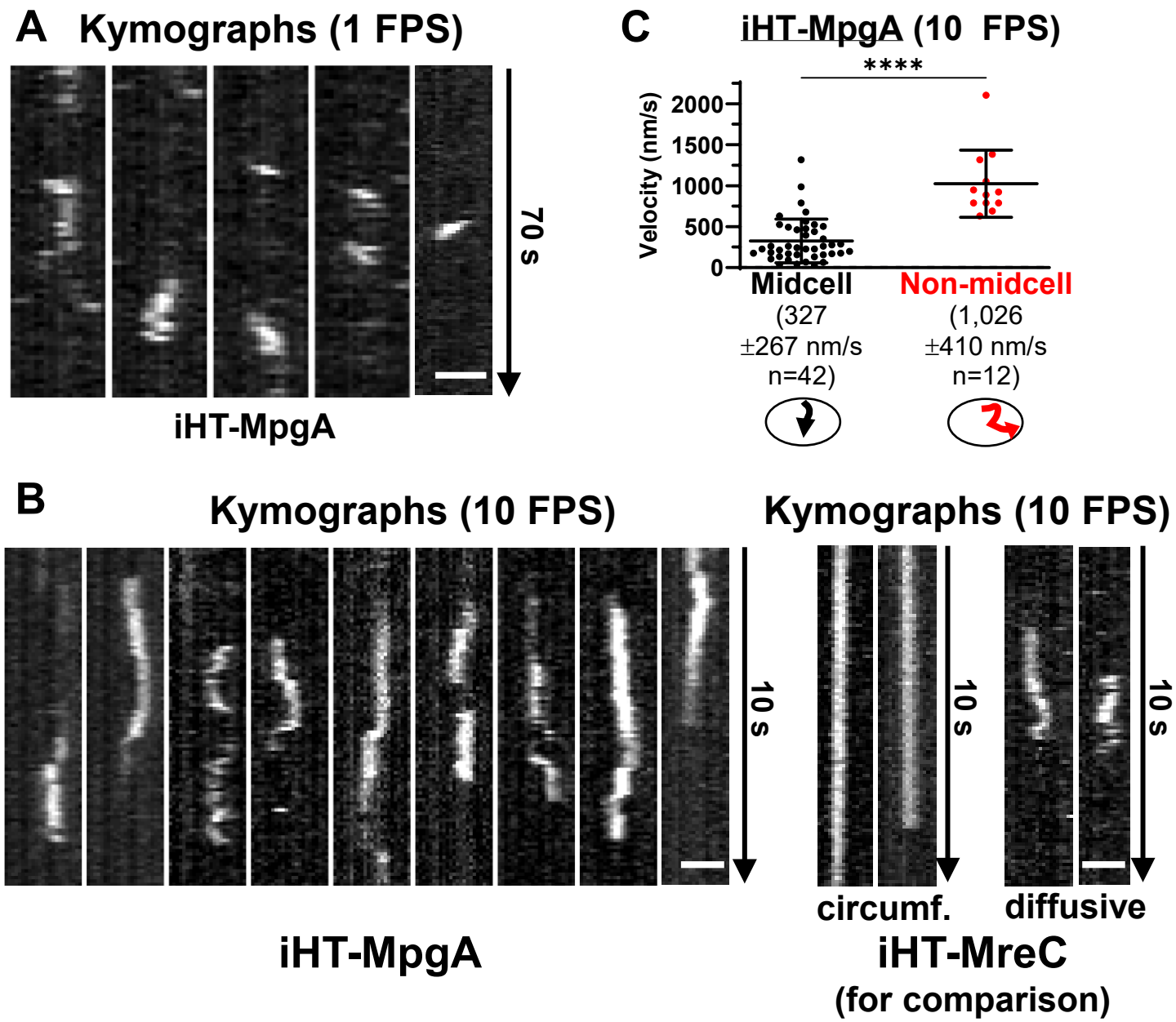

Fig. 9. MpgA displays confined subdiffusive movement at midcell. Sm-TIRFm was performed on strains *iht-mpgA* (IU15997) and *iht-mreC* (IU16344). Representative kymographs of (*A*) iHT-MpgA molecules moving at sites of PG synthesis imaged at 1 FPS and (*B*) iHT-MpgA and iHT-MreC molecules imaged at 10 FPS. (*C*) Dot plots of velocities determined at 10 FPS over short runs of iHT-MpgA molecules in midcell regions (black) and at non-midcell regions (red). Mean values ± SD are indicated. n = total molecules analyzed from 2 biologically independent replicates. Velocities in different regions of cells were compared using a Mann-Whitney test. ****, $P < 0.0001$.

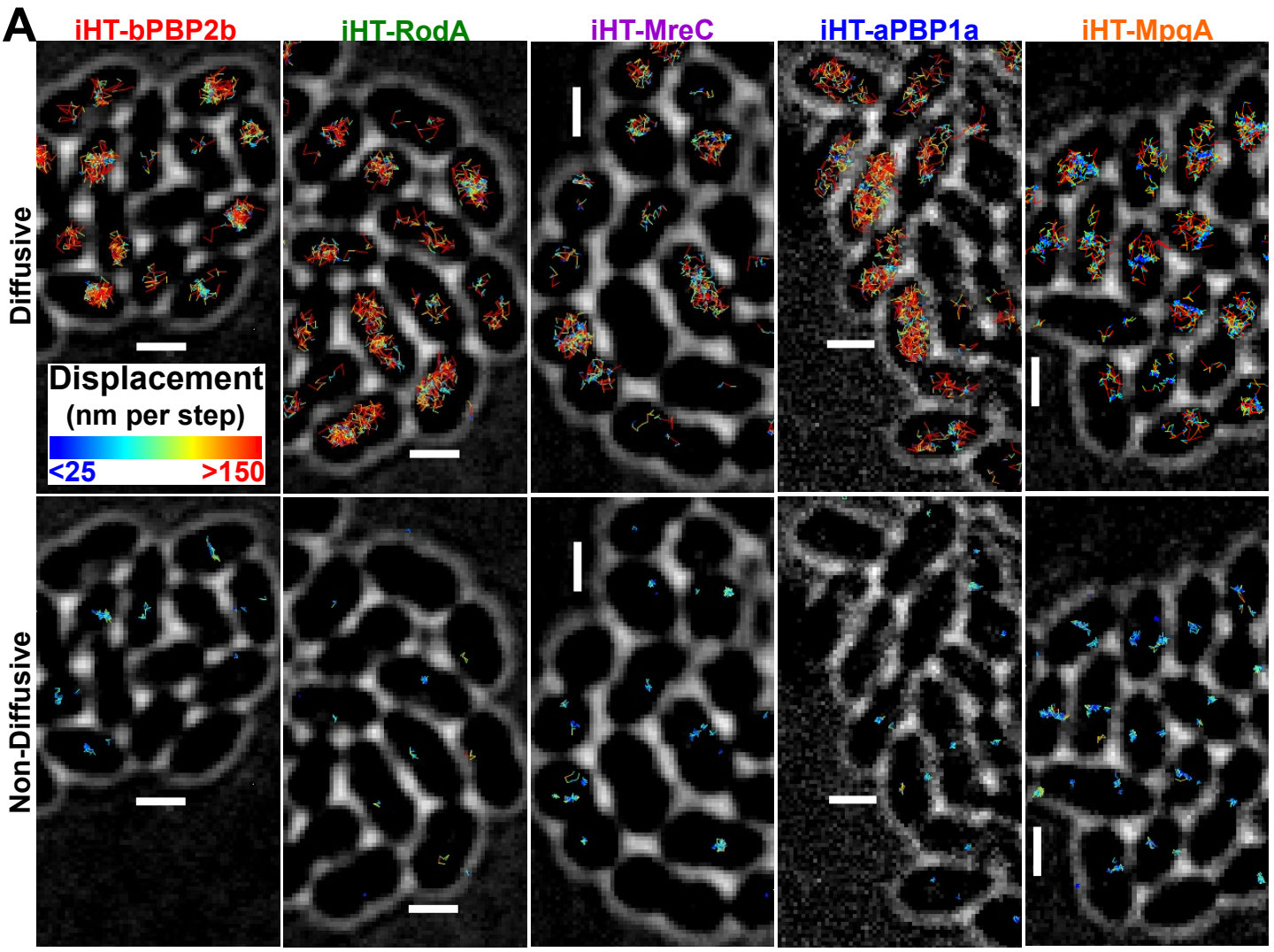

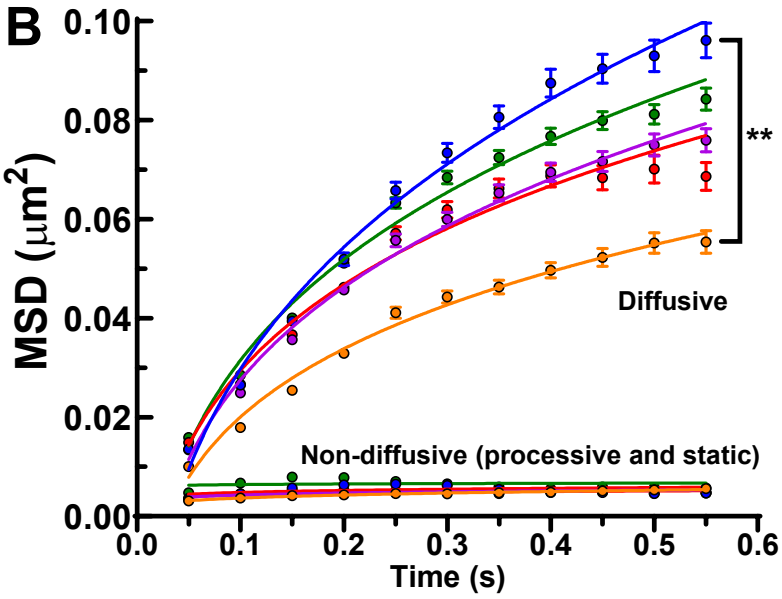

	Diffusion coefficient ($\mu m^2/s$) ±SEM	α	% diffusive	n
iht-pbp1a // P_{Zn}-*iht-pbp1a* +Zn	0.055 ±0.0005	0.28	77	914
iht-rodA // P_{Zn}-*iht-rodA* +Zn	0.050 ±0.0002	0.23	90	2,116
iht-mreC	0.047 ±0.0003	0.22	68	1,351
iht-pbp2b // P_{Zn}-*iht-pbp2b* +Zn	0.046 ±0.0003	0.20	74	1,143
iht-mpgA	0.040 ±0.0003	0.18	60	1,291

Fig. 10.

Fig. 10. Components of the pneumococcal core PG elongasome and proteins implicated in elongation PG synthesis exhibit different patterns of confined diffusion. Sm-TIRFm was performed at 20 FPS on strains *iht-pbp2b* // P_{Zn}-*iht-pbp2b* (IU16553), *iht-rodA* // P_{Zn}-*iht-rodA* (IU16496), *iht-mreC* (IU16344), *iht-pbp1a* // P_{Zn}-*iht-pbp1a* (IU16497) and *iht-mpgA* (IU15997). 0.25 mM Zn inducer was added to strains IU16553, IU16496 and IU16497. (*A*) Representative fields of cells containing multiple single-molecule trajectories (colored lines) classified as diffusive (top row) and non-diffusive (bottom row). Trajectories with a displacement > 0.13 μm and a velocity standard deviation > 0.63 μm/s were defined as diffusive, and the remaining trajectories were defined as non-diffusive. Full details of trajectory constructions and classification criteria are described in *Materials and Methods*. The color of each trajectory line segment represents the displacement (in nm) of the molecule from one frame to the next. Scale bar is 1 μm. (*B*) Mean square displacements (MSD) were calculated for diffusive and non-diffusive trajectories. Circles show MSD values, and error bars represent SEM. Lines represent MSD curves fit to the data as described in *Materials and Methods*. To the right of the graph are the mean diffusion coefficients (± SEM) of diffusive trajectories, alpha values of diffusive trajectories (α), the percent of total trajectories that were classified as diffusive (% diffusive), and the total number of trajectories (n) analyzed from 2 biologically independent replicates. α values < 1 indicate that molecules are exhibiting confined diffusion (or subdiffusion), discussed in the text. The diffusion coefficients were compared between strains using a Brown-Forsythe and Welch's ANOVA with a Games-Howell multiple comparisons test. ** $P < 0.01$.

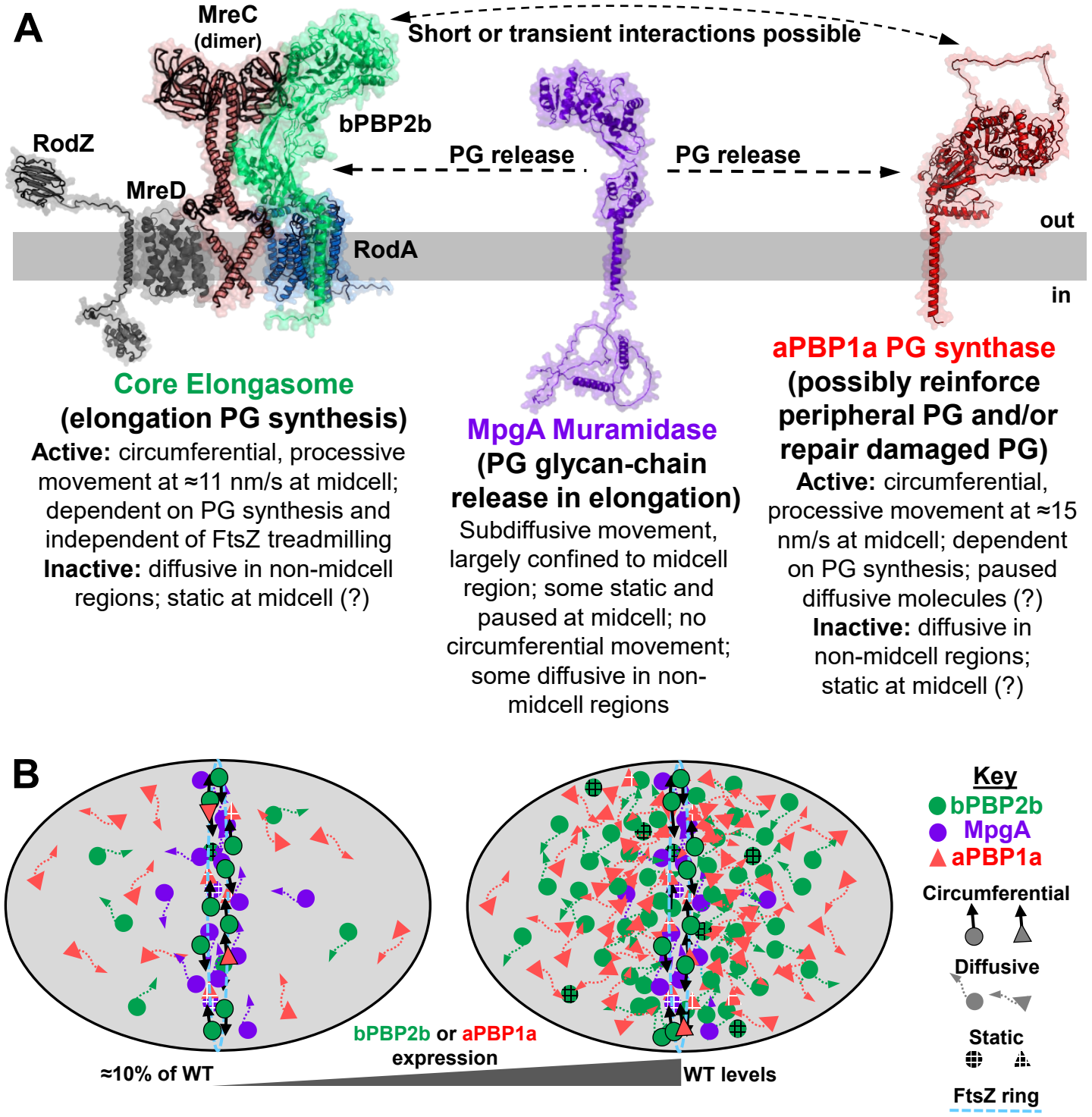
A
MreC
(dimer)
Short or transient interactions possible
bPBP2b
RodZ
PG release
PG release
MreD
out
RodA
in
Core Elongasome
(elongation PG synthesis)
Active: circumferential, processive movement at ≈11 nm/s at midcell; dependent on PG synthesis and independent of FtsZ treadmilling
Inactive: diffusive in non-midcell regions; static at midcell (?)
MpgA Muramidase
(PG glycan-chain release in elongation)
Subdiffusive movement, largely confined to midcell region; some static and paused at midcell; no circumferential movement; some diffusive in non-midcell regions
aPBP1a PG synthase
(possibly reinforce peripheral PG and/or repair damaged PG)
Active: circumferential, processive movement at ≈15 nm/s at midcell; dependent on PG synthesis; paused diffusive molecules (?)
Inactive: diffusive in non-midcell regions; static at midcell (?)
B
bPBP2b or aPBP1a
expression
≈10% of WT
WT levels
Key
bPBP2b
MpgA
aPBP1a
Circumferential
Diffusive
Static
FtsZ ring

Fig. 11.

Fig. 11. Summary model of (*A*) the composition and dynamics of core elongasome components (bPBP2b, RodA, and MreC) and proteins linked to PG elongation synthesis (aPBP1a and MpgA) in growing *S. pneumoniae* cells; and (*B*) the distribution of these proteins when underexpressed (left) or expressed at WT levels (right). (*A*) The circumferential, processive movement of bPBP2b, RodA, and MreC reported here likely apply to the other core elongasome components RodZ and MreD. In early, predivisional cells, the core PG elongasome is located in the FtsZ-ring at the equator midcell of a daughter cell. In later divisional cells, the core PG elongasome is in the outer-ring of the midcell septal annular disk. The motion of MreC is the same in early or late divisional cells. Class A aPBP1a also displays circumferential, processive motion at midcell that depends on PG synthesis, but its dynamics indicate that aPBP1a is not a persistent member of the core PG elongasome, although short interactions are possible. In contrast, MpgA moves in a distinctive type of subdiffusion that is largely confined to the midcell region. Components of the core elongasome and aPBP1a move diffusively outside of midcell rings. There are also nonmoving, static molecules (> 6 s) of elongasome proteins and aPBP1a, mainly in midcell regions. It is not clear whether static molecules are synthesizing PG or are in a non-synthesizing transition state. In addition, diffusing molecules of aPBP1a and MpgA were infrequently detected pausing (< 1s) before resuming motion. See text for additional information. (*B*) When underexpressed, components of the core PG elongasome are largely confined to PG synthesis at midcell septa and the equators of predivisional daughter cells starting to divide. In contrast, when expressed at WT levels, most components of the PG elongasome (and aPBP1a) are diffusing over the cell surface and are not synthesizing PG. Thus, elongasome components and aPBP1a are in excess in growing cells, and only a limited number engage in midcell PG synthesis. In contrast, subdiffusion of MpgA molecules expressed at the WT level is largely confined to the midcell region by an unknown mechanism. See text for additional details.